Plectin Deficiency in Fibroblasts Deranges Intermediate Filament and Organelle Morphology, Migration, and Adhesion

JIDOpen

Michaela M. Zrelski[1], Sabrina Hösele[1], Monika Kustermann[1], Petra Fichtinger[1], Delf Kah[2], Ioannis Athanasiou[3], Philipp R. Esser[3], Anja Wagner[4,5,6], Rebecca Herzog[5,6], Klaus Kratochwill[4,5,6], Wolfgang H. Goldmann[2], Dimitra Kiritsi[3] and Lilli Winter[1]

Plectin, a highly versatile and multifunctional cytolinker, has been implicated in several multisystemic disorders. Most sequence variations in the human plectin gene (*PLEC*) cause epidermolysis bullosa simplex with muscular dystrophy (EBS-MD), an autosomal recessive skin-blistering disorder associated with progressive muscle weakness. In this study, we performed a comprehensive cell biological analysis of dermal fibroblasts from three different patients with EBS-MD, where *PLEC* expression analyses revealed preserved mRNA levels in all cases, whereas full-length plectin protein content was significantly reduced or completely absent. Downstream effects of pathogenic *PLEC* sequence alterations included massive bundling of vimentin intermediate filament networks, including the occurrence of ring-like nuclei-encasing filament bundles, elongated mitochondrial networks, and abnormal nuclear morphologies. We found that essential fibroblast functions such as wound healing, migration, or orientation upon cyclic stretch were significantly impaired in the cells of patients with EBS-MD. Finally, EBS-MD fibroblasts displayed reduced adhesion capacities, which could be attributed to smaller focal adhesion contacts. Our study not only emphasizes plectin's functional role in human skin fibroblasts, it also provides further insights into the understanding of EBS-MD–associated disease mechanisms.

Journal of Investigative Dermatology (2023) ■, ■–■; doi:10.1016/j.jid.2023.08.020

INTRODUCTION

Epidermolysis bullosa (EB) comprises a group of heritable skin fragility disorders with a highly heterogeneous genetic and clinical spectrum (Vahidnezhad et al., 2019). On the basis of the area of blister formation, EB is subdivided into four groups comprising EB simplex (EBS), junctional EB, dystrophic EB, and Kindler EB (Has et al., 2020). In EBS, tissue separation occurs in an intraepidermal fashion owing to cleavage within the basal layer of keratinocytes (KCs), provoking the detachment of the upper parts of the epidermis from underlying skin layers. Among the seven classical EBS-causing genes reported so far (Has et al., 2020), one deserves special attention owing to unique extracutaneous disease manifestations. Most sequence variations in the human plectin gene (*PLEC*) on chromosome 8q24 (Liu et al., 1996) cause autosomal recessive EBS with muscular dystrophy (EBS-MD) (Mendelian Inheritance in Man #226670), where the congenital skin-blistering phenotype is accompanied by a late onset of progressive muscle weakness. Subsumed under the term plectinopathies, diseases caused by *PLEC* alterations encompass a multitude of clinical entities, frequently displaying multisystemic symptoms, for example, EBS can be associated with a myasthenic syndrome, pyloric atresia, or nail dystrophy. The autosomal-dominant disorder EBS-Ogna, aplasia cutis congenita, limb-girdle muscular dystrophy (LGMDR17), and cardiomyopathies add to the complex manifestations of human plectinopathies (Kiritsi et al., 2021; Vahidnezhad et al., 2022; Zrelski et al., 2021).

The *PLEC* locus, consisting of 43 exons, gives rise to an exceptionally large (>500 kDa) and multifunctional cytolinker protein. By interacting with actin, microtubules, and intermediate filaments (IFs), plectin associates with all three major cytoskeletal filament systems and anchors them to sites of strategic importance for the function and organization of cells (Wiche and Winter, 2011). A highly conserved actin-binding domain and a plakin domain, providing among other direct binding sites for actin and microtubule-associated proteins, have been mapped on the N-terminal globular domain, whereas the major interaction site for all types of IF subunit proteins was located on the C-terminal

[1]*Department of Cell and Developmental Biology, Center for Anatomy and Cell Biology, Medical University of Vienna, Vienna, Austria;* [2]*Center for Medical Physics and Technology, Department of Physics, Friedrich-Alexander-University Erlangen-Nuremberg, Erlangen, Germany;* [3]*Department of Dermatology, Medical Center University of Freiburg, Faculty of Medicine, University of Freiburg, Freiburg, Germany;* [4]*Core Facility Proteomics, Medical University of Vienna, Vienna, Austria;* [5]*Division of Pediatric Nephrology and Gastroenterology, Department of Pediatrics and Adolescent Medicine, Comprehensive Center for Pediatrics, Medical University of Vienna, Vienna, Austria; and* [6]*Christian Doppler Laboratory for Molecular Stress Research in Peritoneal Dialysis, Division of Pediatric Nephrology and Gastroenterology, Department of Pediatrics and Adolescent Medicine, Comprehensive Center for Pediatrics, Medical University of Vienna, Austria*

Correspondence: Lilli Winter, Department of Cell and Developmental Biology, Center for Anatomy and Cell Biology, Medical University of Vienna, Währingerstrasse 13, Vienna 1090, Austria. E-mail: lilli.winter@meduniwien.ac.at

Abbreviations: AS, antiserum; EB, epidermolysis bullosa; EBS, epidermolysis bullosa simplex; EBS-MD, epidermolysis bullosa simplex with muscular dystrophy; IF, intermediate filament; KC, keratinocyte; PTC, premature termination codon; siRNA, small interfering RNA

Received 20 April 2023; revised 3 August 2023; accepted 9 August 2023; accepted manuscript published online XXX; corrected proof published online XXX

IF-binding domain. N- and C-terminal globular domains are connected by a central α-helical rod domain, which forms a ~200 nm long coiled-coil upon dimerization (Foisner and Wiche, 1987). In addition, alternatively spliced first coding exons ensure plectin's role as a universal recruiter of filament networks because they enable differential targeting to distinct subcellular locations. Specific filament anchorage occurs on several cytoskeletal junctional complexes, including focal adhesions, hemidesmosomes, desmosomes, adherens- and β-dystroglycan junctions, the neuromuscular synapse, and invadopodia of metastatic cancer cells as well as at the cytoplasmic face of organelles, particularly on mitochondria and the nuclear/endoplasmic reticulum membrane (Fuchs et al., 1999; Rezniczek et al., 2003; Wiche, 2021). In addition, plectin exceeds its pure networking function by interacting with several kinases of known roles such as migration, proliferation, and energy metabolism (Castañón et al., 2013).

The concept that plectin primarily confers mechanical stability is highly supported by its expression pattern because it is particularly abundant in tissues challenged by high mechanical demands such as skin and muscle. In EBS-MD, the skin blistering has been attributed at the molecular level to a disruption of the normal keratin IF anchorage to hemidesmosomes (Gache et al., 1996; Koster et al., 2004). In skeletal muscle, the extrasarcomeric desmin IF cytoskeleton is destructed, leading to the accumulation of desmin-positive protein aggregates and loss of sarcomere organization (Winter et al., 2016; Zrelski et al., 2021). To a lesser extent, plectin is universally expressed in virtually all cell types and tissues examined so far (Castañón and Wiche, 2021; Fuchs et al., 1999). Since its molecular identification ~40 years ago, diverse ultrastructural, biochemical, immunological, and molecular studies contributed to our current knowledge about plectin's central role in the organization and performance of vertebrate cells (Castañón and Wiche, 2021; Wiche, 2021). Although the first insights into the function of plectin in vivo came from patients with *PLEC* alterations, great parts of our knowledge about plectin's diversity have been gained through the analysis of transgenic animal models and cells derived from them (Castañón and Wiche, 2021).

However, despite its clear clinical relevance, data from patient-derived plectinopathic cells are scarce, and only a few studies have addressed plectin mRNA and/or protein expression in KCs, myoblasts, amniocytes, or fibroblasts from patients with *PLEC* alterations (Bauer et al., 2001; Chavanas et al., 1996; Gache et al., 1996; Gostyńska et al., 2017, 2015; Koss-Harnes et al., 2004; Martínez-Santamaría et al., 2022; McLean et al., 1996; Nakamura et al., 2011; Natsuga et al., 2017, 2010a, 2010b; Schröder et al., 2002; Yiu et al., 2011). Considering the plethora of additional clinical manifestations in plectinopathies such as impaired wound-healing or scarring (Kyrova et al., 2016), a functional involvement of human skin fibroblasts in the disease pathomechanisms is highly anticipated. However, important questions regarding the mechanistic effects of individual *PLEC* alterations as well as their impact on fibroblast functions remained unanswered. For instance, what are the consequences of the respective *PLEC* alterations on mRNA and protein expression levels as well as the subcellular localization of plectin itself and on the cytoskeletal filaments systems such as actin fibers, microtubules, and vimentin IFs? Are cell shape, size, or cellular organelles (e.g., mitochondria, nuclei) altered in fibroblasts derived from patients with EBS-MD when compared with those of healthy controls? Furthermore, it is largely unknown whether *PLEC* alterations affect basal fibroblast properties such as migration or adhesion.

Addressing these and other relevant aspects in this study, we elaborately characterized dermal fibroblasts derived from three different patients with EBS-MD with previously reported *PLEC* alterations (Bauer et al., 2001; Kunz et al., 2000; Natsuga et al., 2010a). We found especially IFs hugely altered upon *PLEC* alteration as bundling of vimentin filaments and increased appearance of vimentin rings around the nuclei became apparent in EBS-MD fibroblasts. In addition, elongated mitochondria and distorted nuclear morphologies accompanied by altered protein expression levels of nuclear proteins such as emerin or LAP2α emphasize additional cellular pathological hallmarks related to *PLEC* alterations. Finally, focusing on functional aspects, we found diminished migration and wound-healing capacities, reduced orientation after application of cyclic stretch, and impaired adhesion of EBS-MD fibroblasts. In summary, our study emphasizes plectin's functional role in human skin fibroblasts and highlights their relevance for cutaneous disorders.

RESULTS

Characterization and plectin expression of fibroblasts from patients with EBS-MD

To explore the functional consequences of sequence variations in the human *PLEC* gene on a cellular level, primary human dermal fibroblasts were obtained from two patients with EBS-MD carrying previously reported compound heterozygous allelic variants, all resulting in premature termination codons (PTCs) within the central rod domain-encoding exon 31 (Figure 1a and Supplementary Table S1). In addition, immortalized fibroblasts from a third patient with EBS-MD with a compound heterozygous one amino-acid insertion in exon 9 and a nonsense mutation in exon 31 of *PLEC* (Bauer et al., 2001; Wally et al., 2008) were included in the analyses. Homogenous populations of control fibroblasts that have been derived from cells from healthy individuals and patients with EBS-MD presented similar morphology (Supplementary Figure S1a), and no significant alterations in cell area, perimeter, aspect ratio, circularity, or roundness were observed (Supplementary Figure S1b).

To assess the direct consequences of *PLEC* alterations, we evaluated plectin mRNA and protein expression levels using RT-qPCR and immunoblotting analyses. Previous experiments indicated that normal human fibroblasts expressed two different *PLEC* versions: (i) full-length plectin, ranging from any of the alternatively spliced first exons to exon 32 and (ii) shorter variants, lacking the rod domain-encoding exon 31 denoted as rodless plectin (Natsuga et al., 2010a) (Figure 1a). Accordingly, distinct primer combinations were used in RT-qPCR experiments, specifically amplifying plectin variants. In this experiment, no significant differences were observed for the amplification of full-length and

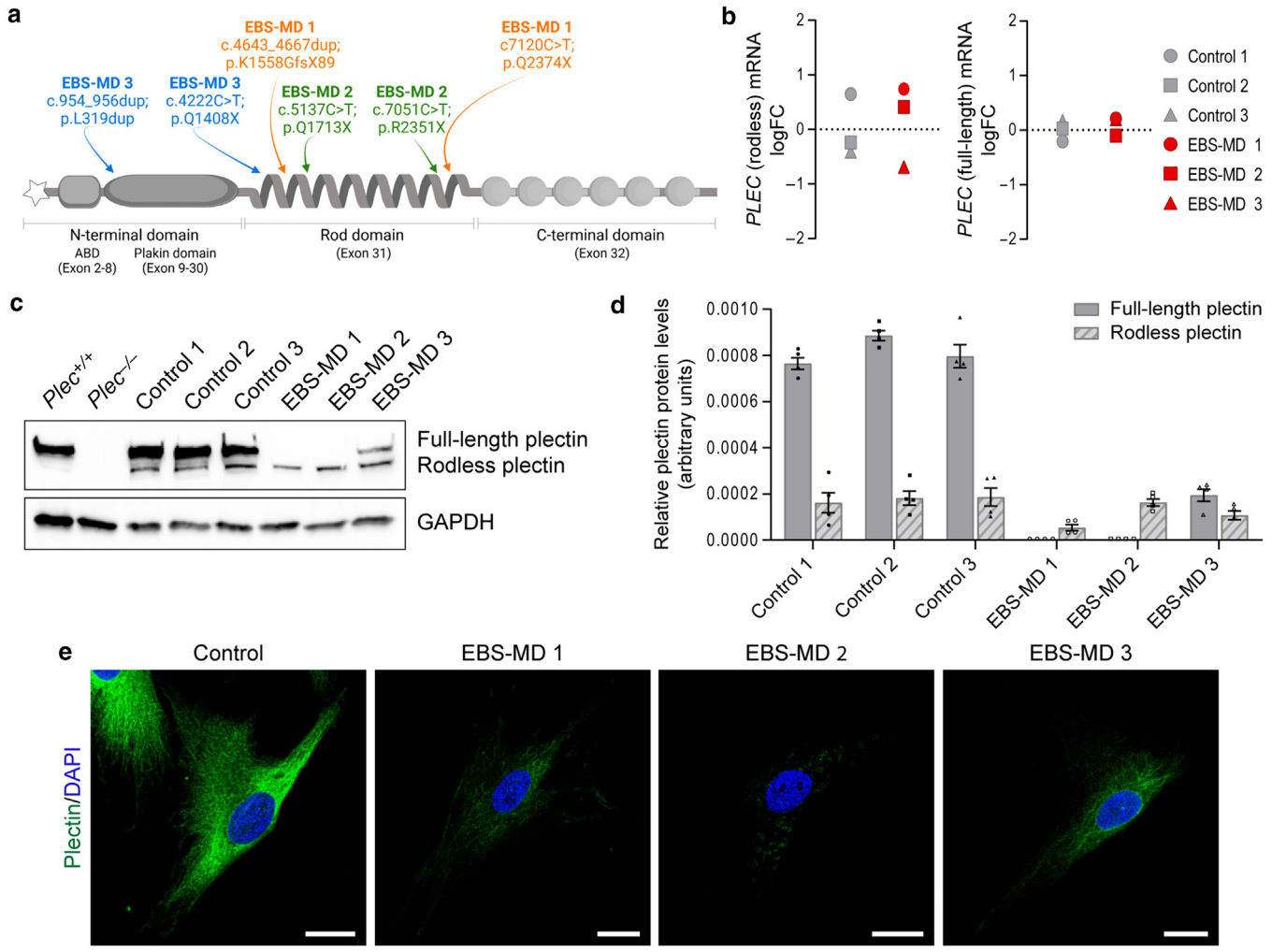

Figure 1. Schematic representation of the *PLEC* alterations, plectin mRNA, and protein expression in EBS-MD fibroblasts. (**a**) Schematic domain map of plectin and positional mapping of the EBS-MD alterations. The tripartite structure of the plectin molecule consists of a central, α-helical rod domain, which is flanked by N- and C-terminal globular domains, containing actin-binding and plakin domain, or six homologous plectin-repeat domains. The different N termini of the individual plectin isoforms are indicated by a star. Note that alternative splicing of exon 31 results in the expression of rodless plectin protein. Further note that whereas compound heterozygous allelic variants in exon 31 have been identified for patients 1 and 2 with EBD-MD, patient 3 with EBS-MD harbors compound heterozygous alterations in exons 9 and 31. (**b**) RT-qPCR analyses of rodless and full-length plectin (*PLEC*) mRNA expression. Relative gene expression values are depicted as logFC and were normalized to *TBP* and *RPLP0*. Samples were measured as triplicates. (**c**) Immunoblotting of cell lysates prepared from murine plectin-positive ($Plec^{+/+}$) and plectin-deficient ($Plec^{-/-}$) as well as human control and EBS-MD fibroblasts using antibodies to plectin. GAPDH was used as the loading control. Note that whereas no full-length plectin bands could be detected in fibroblasts from patients 1 and 2 with EBS-MD, markedly reduced but still recognizable plectin levels were observed in fibroblasts from patient 3 with EBS-MD. Furthermore, note the detection of rodless plectin in all EBS-MD and control lysates. (**d**) Signal intensities of full-length and rodless plectin protein bands as shown in **c** were densitometrically measured and normalized to the total protein content as assessed by Coomassie staining (not shown). Data are presented as mean ± SEM; n = 4, derived from two independent experiments (at two different passages). (**e**) Immunostaining of control and EBS-MD fibroblasts using antiplectin antibodies and visualization of nuclei (DAPI). Bars = 20 μm. EBS-MD, epidermolysis bullosa simplex with muscular dystrophy; logFC, $\log_2$ fold change.

rodless plectin mRNA transcripts from EBS-MD or control fibroblasts (Figure 1b), indicating similar levels of *PLEC* transcription in both cell types. In plectin immunoblot analyses of fibroblast lysates, two bands were detected: one with a strong signal intensity corresponding to a molecular mass of ~500 kDa and a second, fainter signal at ~390 kDa representing full-length and rodless plectin variants in all control samples (Figure 1c). Cell lysates from patients 1 and 2 with EBS-MD displayed complete absence, whereas patient 3 with EBS-MD presented markedly reduced full-length plectin protein levels. Contrary to that, expression of rodless plectin variants was preserved in all three patients with EBS-MD, albeit to a different extent. Statistical evaluations of band signals revealed a drastic reduction of full-length plectin protein to ~24% in patient 3 with EBS-MD, whereas rodless plectin protein levels remained similar to those of control samples in patient 2 with EBS-MD but were reduced to ~30 and ~60% in patients 1 and 3, respectively (Figure 1d). Finally, when evaluated by immunofluorescence microscopy, control fibroblasts presented delicate and widespread filamentous plectin networks throughout the cytoplasm, whereas the specimens from patients with EBS-MD displayed markedly reduced plectin staining (Figure 1d). Thus, albeit displaying

differences between individual patients, the *PLEC* alterations led to a drastic reduction in plectin protein levels.

Impact of *PLEC* alterations on the cytoskeleton of human fibroblasts: formation of vimentin IF bundles and nuclei-encasing ring-like structures

Because plectin's primary function as a cytolinker protein is the interlinkage and anchorage of the three major cytoskeletal filament systems, we assessed mRNA expression, protein levels, and subcellular distribution of actin filaments, microtubules, and vimentin IFs. Using RT-qPCR, we found no significant differences in the mRNA levels of *ACTB*, *TUBA1B*, and *VIM* between EBS-MD fibroblasts and control cells (Figure 2a and Supplementary Figures S2a and S3a). Likewise, immunoblot analyses of cell lysates revealed no differences in β-actin, α-tubulin, or vimentin protein levels (Figure 2b and c; Supplementary Figures S2b and c and S3b and c). To compare the general appearance of cytoskeletal networks, 24 hour–plated cells were stained for F-actin using phalloidin and for microtubules and IFs using antibodies to α-tubulin or vimentin, respectively. Interestingly, although no obvious differences were observed for actin (Supplementary Figure S2d) or tubulin (Supplementary Figure S3d), vimentin IFs appeared densely packed and more bundled in the patients' fibroblasts (Figure 2d). In addition, in EBS-MD cells, these cable-like vimentin bundles often formed prominent ring-like structures around the nuclei (Figure 2e), whereas in the periphery, the IF networks presented enlarged mesh size, thereby leaving areas devoid of vimentin (Figure 2f). Although ∼61% of EBS-MD cells harbored prominent vimentin rings, only ∼10% of control cells were found with these structures (Figure 2g). Notably, increased bundling of IF filaments and the occurrence of vimentin rings were observed in all EBS-MD cultures irrespective of the actual passage number (data not shown). Fluorescence intensity plots of IFs in peripheral areas reinforce the observation of collapsed, dense bundles in EBS-MD fibroblasts without any filaments between them, whereas in the periphery of control cells, delicate vimentin networks almost fill the entire cytoplasm (Figure 2h). To address the question of whether the observed vimentin reorganization was directly provoked by a loss of plectin protein, immortalized plectin-deficient ($Plec^{-/-}$) fibroblasts (derived from plectin-null mice) and plectin-positive ($Plec^{+/+}$) controls were stained for vimentin and evaluated in a similar way (Supplementary Figure S4a–c). Strikingly, $Plec^{-/-}$ cells also displayed prominent nuclear vimentin rings (Supplementary Figure S4b and d) and highly collapsed IF bundles (Supplementary Figure S4c and e). Consequently, small interfering RNA (siRNA) knockdown of plectin in human control fibroblasts also induced the occurrence of nuclei-encasing vimentin bundles (Supplementary Figure S4f–h).

To test whether the observed alterations in IF network structure affected its resistance to high-salt and -detergent extraction, the solubility (extractability) of vimentin from control and EBS-MD cell lysates was assessed (Figure 2i). Notably, vimentin solubility was found increased by approximately threefold in EBS-MD lysates compared with that in control samples (Figure 2j). Because site-specific phosphorylation induces disassembly of vimentin filaments, we evaluated whether vimentin differs between EBS-MD fibroblasts and control cells by employing two-dimensional gel electrophoresis of cell lysates combined with immunoblotting using antibodies to vimentin. Thereby, individual vimentin species harboring different post-translational modifications, including phosphorylation, can be separated and visualized (Supplementary Figure S5). In addition, we performed a full-mass spectrometric analysis of cell lysates and specifically searched for vimentin phosphorylation sites (Supplementary Table S2). Strikingly, in both the top-down and the bottom-up approaches, no obvious differences in vimentin phosphorylation were observed between controls and EBS-MD fibroblasts. Collectively, these data support the notion that *PLEC* alterations, although leaving actin and microtubule networks largely unaltered, imply drastic structural and organizational changes in the vimentin IF cytoskeleton.

PLEC alterations lead to altered mitochondrial and nuclear morphologies in human fibroblasts

Previous findings of altered organelle and/or nuclear morphology in various plectin-deficient mouse cells (Almeida et al., 2015; Staszewska et al., 2015; Winter et al., 2015, 2008) prompted us to investigate mitochondria and nuclei in EBS-MD fibroblasts. We therefore first monitored the shape of mitochondrial networks using cytochrome c–specific immunostaining (Figure 3a) and classified them as fragmented, intermediate, or elongated (Winter et al., 2008). Interestingly, although 14, 80, and 6% of mitochondria presented fragmented, intermediate, or elongated morphologies in control cells, respectively, almost 20% of EBS-MD fibroblasts displayed elongated organelles, whereas the fragmented type was reduced to 2%, indicating a dramatic shift from the small and fragmented type to the elongated organelle form (Figure 3b). To examine whether these differences were due to altered electron transport chain composition, the levels of electron transport complex proteins such as ATP5A, UQCRC2, SDHB, COXII, and NDUFB8 were assessed by immunoblotting (Figure 3c), though without any significant differences between EBS-MD and control cells (Figure 3d).

Next, we assessed nuclear morphologies of DAPI-stained control and EBS-MD fibroblasts (Figure 4a) and counted nuclei displaying irregular shapes (Figure 4b) (EBS-MD 3) or dramatically deformed morphologies, including the occurrence of nuclear blebs (Figure 4b) (EBS-MD 1 and EBS-MD 2) (Lammerding et al., 2005). Strikingly, whereas 25% of EBS-MD fibroblasts harbored blebbing nuclei, such alterations were only observed in 5% of control cells (Figure 4c). To further analyze the consequences of *PLEC* alterations, the levels of nuclear components such as IF protein lamin A/C, LAP2α, or emerin were analyzed by immunoblotting (Figure 4d). In patient 3 with EBS-MD, our measurements revealed a tendency toward decreased lamin A protein level however without reaching statistical significance (Figure 4e). LAP2α protein levels were found drastically increased in patient 2 with EBS-MD and reduced in patient 3 with EBS-MD while being similar in the controls and patient 1 with EBS-MD. Strikingly, in all lysates from patients with EBS-MD, the emerin protein level was significantly reduced

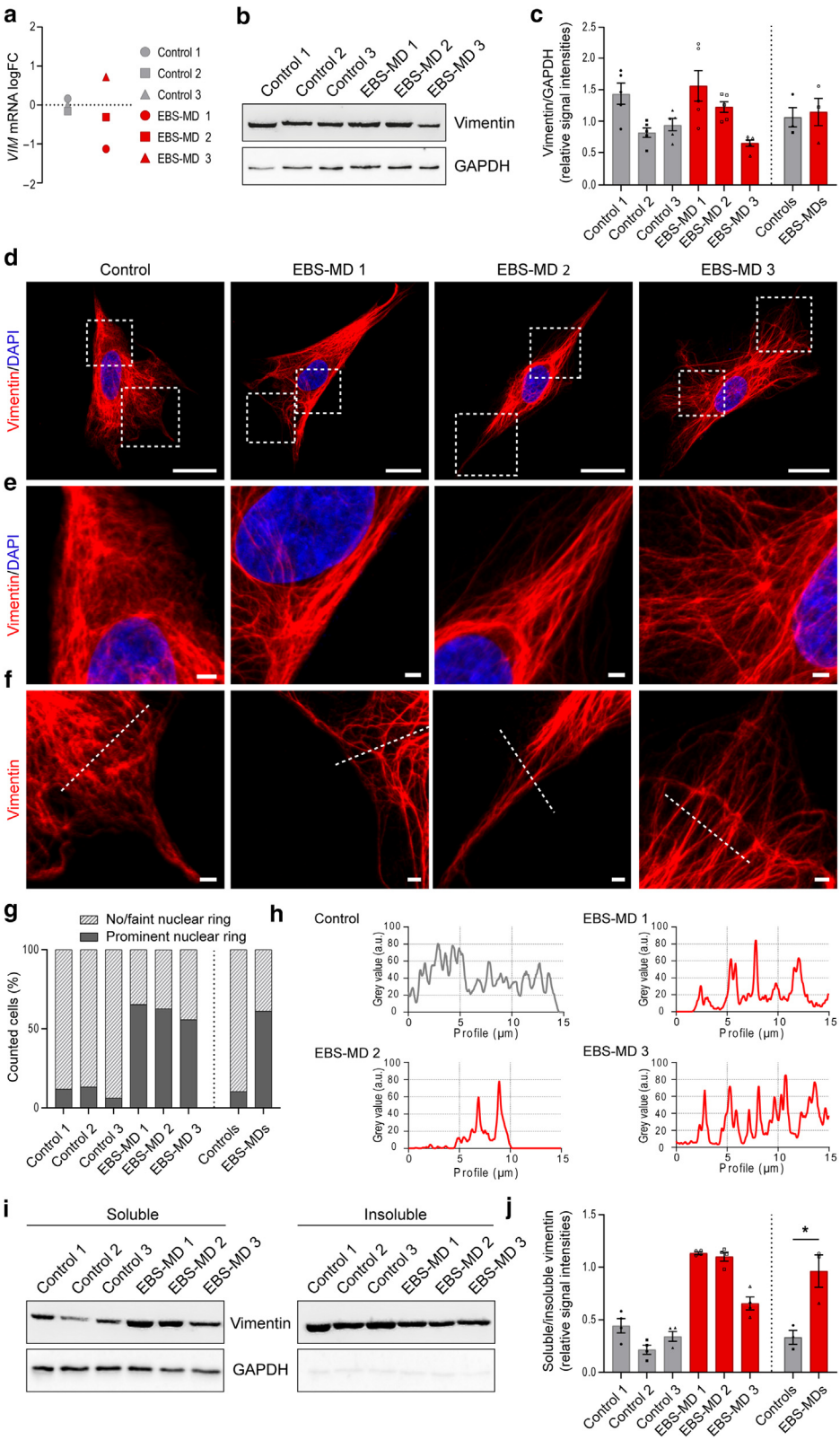

Figure 2. Altered intermediate filament network architecture and increased solubility of vimentin in EBS-MD fibroblasts. (**a**) RT-qPCR analyses of vimentin (*VIM*) mRNA expression. Relative gene expression values are depicted as logFC and were normalized to *TBP* and *RPLP0*. Samples were measured as triplicates. (**b**) Immunoblotting of cell lysates prepared from control and EBS-MD fibroblasts using antibodies to vimentin. GAPDH was used as the loading control. (**c**) Signal intensities of vimentin protein bands as shown in **b** were densitometrically measured and normalized to GAPDH. Data are presented as mean ± SEM; n = 5, derived from two independent experiments (at two different passages). (**d**–**f**) Immunostaining of control and EBS-MD fibroblasts using antibodies to vimentin and visualization of nuclei (DAPI, for **d**). Boxes indicated in **d** are magnified in **e** and **f**. Note the (**e**) formation of ring-like nuclei-encasing structures and (**f**) highly bundled cable-like vimentin IFs in EBS-MD fibroblasts. Bars = 20 µm (for **d**) and 2 µm (for **e** and **f**). (**g**) Percentage of fibroblasts with or without a prominent nuclear vimentin IF ring; control 1 (n = 77 cells), control 2 (n = 84 cells), control 3 (n = 66 cells), EBS-MD 1 (n = 72 cells), EBS-MD 2 (n =

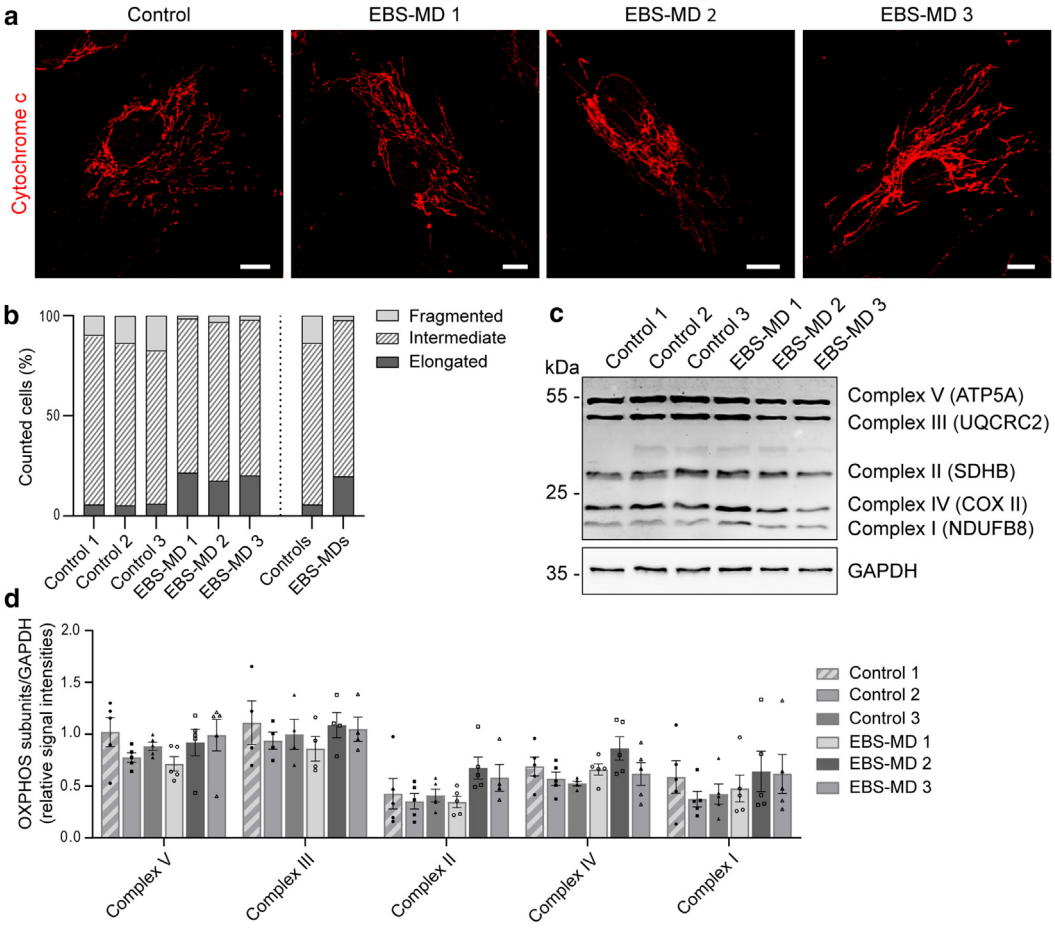

Figure 3. Elongated mitochondria in EBS-MD fibroblasts. (**a**) Confocal images of mitochondrial network organization on control and EBD-MD fibroblasts visualized by immunostaining using antibodies to cytochrome c. Nuclei were stained with DAPI. Bars = 20 μm. (**b**) Percentage of cells presenting with fragmented, intermediate, or elongated mitochondria (Winter et al., 2008) (control 1 [n = 124 cells], control 2 [n = 133 cells], control 3 [n = 132 cells], EBS-MD 1 [n = 144 cells], EBS-MD 2 [n = 126 cells], and EBS-MD 3 [n=139 cells]). (**c**) Immunoblotting of cell lysates prepared from control and EBS-MD fibroblasts using antibodies specific for components of the electron transport chain complexes I–V. GAPDH was used as the loading control. (**d**) Signal intensities of protein bands of complexes I–V as shown in **c** were densitometrically measured and normalized to GAPDH. Data are presented as mean ± SEM, n = 4–6 data points, derived from two independent experiments (at two different passages). EBS-MD, epidermolysis bullosa simplex with muscular dystrophy.

compared with that in the control samples (Figure 4e and f). Lamin A/C–specific immunostaining uncovered additional nuclear malformations such as honeycomb structures or donut shapes (Stiekema et al., 2020; van Tienen et al., 2019) in all EBS-MD fibroblasts (Figure 4g and Supplementary Figure S6a), whereas LAP2α and emerin localized in a similar way in all cells (Supplementary Figure S6b). Because murine *Plec*$^{-/-}$ fibroblasts also displayed significantly increased amounts of misshaped nuclei (Supplementary Figure S6c–e) and reduced emerin protein levels compared with *Plec*$^{+/+}$ cells, these nuclear phenotypes could be directly attributed to a loss of plectin protein (Supplementary Figure S6f and g). Thus, *PLEC* alterations provoke morphological aberrations of mitochondria and nuclei and differentially affect the expression of certain nuclear proteins, without a clear profile in the EBS-MD fibroblasts tested.

Impact of *PLEC* alterations on fibroblast functions: reduced wound healing, impaired migration, and adhesion

Skin blister formation, a major hallmark of EBS-MD (Kiritsi et al., 2021), requires the consequent repair of wounds to preserve the physiological and mechanical properties of the skin and to restore its barrier function. Dermal fibroblasts, migrating into the wound, trigger the proliferative phase of wound healing, which ultimately leads to increased production of extracellular matrix components (Amiri et al., 2022). To investigate whether basic fibroblast functions,

72 cells), EBS-MD 3 (n = 70 cells). (**h**) Graphs represent fluorescence intensity profiles illustrating the respective vimentin distributions in control and EBS-MD fibroblasts. The white dashed lines in **f** denote the direction of the profiling. Note the formation of prominent individual peaks and distinct spaces devoid of vimentin signals in EBS-MD fibroblasts. (**i**) Immunoblotting of equal amounts of soluble and insoluble fractions derived from control and EBS-MD fibroblasts using antibodies to vimentin. GAPDH was used as the loading control. (**j**) Signal intensities for soluble and insoluble vimentin protein bands as shown in **i** were densitometrically measured, and the ratio of soluble versus insoluble vimentin was statistically evaluated. Data are presented as mean ± SEM; n = 4 technical replicates. *$P < 0.05$, unpaired Student's *t*-test. EBS-MD, epidermolysis bullosa simplex with muscular dystrophy; IF, intermediate filament; logFC, $\log_2$ fold change.

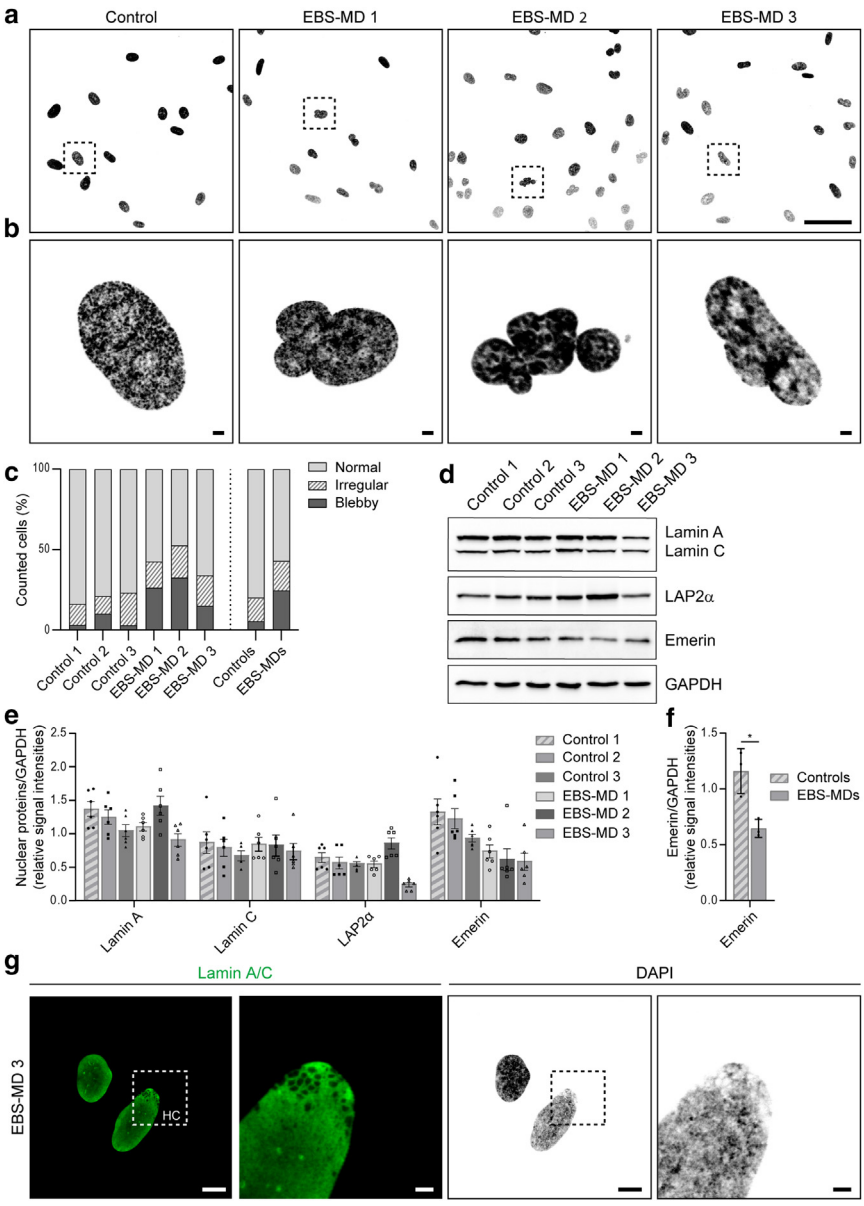

Figure 4. Altered nuclear morphology in EBS-MD fibroblasts. (**a**) Visualization of nuclear morphology (DAPI) in control and EBD-MD fibroblasts. (**b**) Magnifications of the boxed nuclei in **a**. Note the occurrence of nuclear abnormalities such as irregularly shaped nuclei (EBS-MD 3) and nuclei with blebs (EBS-MD1 and EBS-MD 2). Bars = 50 μm (for **a**) and 2 μm (for **b**). (**c**) Percentage of cells presenting with normal, irregularly shaped, or blebbing nuclei (Lammerding et al., 2005) (control 1 [n = 99 cells], control 2 [n = 119 cells], control 3 [n = 104 cells], EBS-MD 1 [n = 134 cells], EBS-MD 2 [n = 120 cells], and EBS-MD 3 [n = 133 cells]). (**d**) Immunoblotting of cell lysates prepared from control and EBS-MD fibroblasts using antibodies to nuclear proteins. GAPDH was used as the loading control. (**e**) Signal intensities of protein bands of lamin A, lamin C, LAP2α, and emerin as shown in **d** were densitometrically measured and normalized to GAPDH. Data are presented as mean ± SEM, n = 6 data points, derived from two independent experiments (at two different passages). Note that LAP2α protein levels, although similar in the controls and cell lysates from patient 1 with EBS-MD, appeared drastically increased in patient 2 with EBS-MD and reduced in patient 3 with EBS-MD. In addition, note that emerin protein levels appeared reduced in all EBS-MD fibroblast samples compared with those in control cells. (**f**) Statistical evaluation of emerin protein levels in controls versus EBS-MD patients. Data are presented as mean ± SEM, three experiments. $*P < 0.05$, unpaired Student's *t*-test. (**g**) Immunostaining of fibroblasts from patient 3 with EBS-MD using antibodies to lamin A/C. Nuclei were stained with DAPI. Insets are magnifications of the nuclear areas as indicated by the boxes. Note that the honeycomb structures (denoted as HC) (van Tienen et al., 2019) in the nuclear lamina are particularly evident in this single-plane view derived from a confocal Z-stack (see also Supplementary Figure S6a), combined with a reduction of DNA staining in the same area. Bars = 10 μm and 2 μm (magnifications). EBS-MD, epidermolysis bullosa simplex with muscular dystrophy.

such as migration, were altered with plectin deficiency, the migratory abilities of EBS-MD fibroblasts were assessed in an in vitro wound-healing assay. Therefore, a confluent cell monolayer was mechanically scratched, and the movement of cells into the empty space was monitored over a period of 48 hours (Figure 5a). After 9 or 24 hours, control cells had already closed 25 or 90% of the scratch area, respectively, whereas EBS-MD fibroblasts showed significantly impaired migration, leaving 50% of the wound area still open after 24 hours (Figure 5b). However, 48 hours after wounding, both cell types were able to reach confluency again, suggesting that EBS-MD fibroblasts were still able to exert wound-

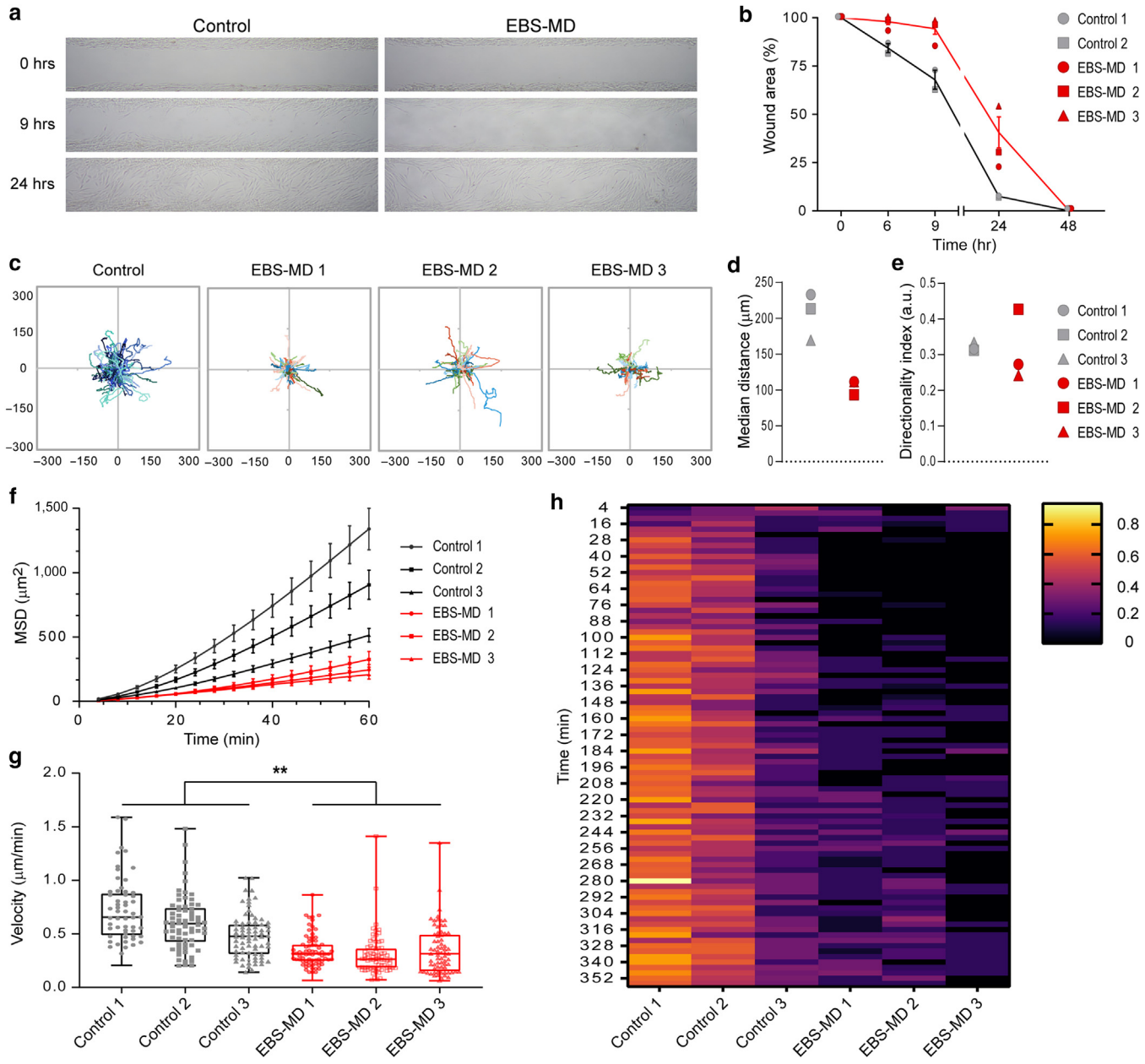

Figure 5. Reduced wound healing and impaired random migration of EBS-MD fibroblasts. (**a**) Representative bright-field images of control and EBS-MD fibroblasts unwounded and 9 and 24 hours after wounding. (**b**) Statistical analysis of the scratch-wound closure monitored over time. Data are presented as mean ± SEM. (**c**) Flower plots presenting the trajectories of control and EBS-MD fibroblasts obtained in a single-cell motility assay within 6 hr. (**d**) Statistical evaluation of the median distances moved by control and EBS-MD cells and (**e**) calculation of the directionality indices according to Gorelik and Gautreau (2014). (**f**) Analysis of the MSD of control and EBS-MD fibroblasts assessed over the initial 60 minutes of monitoring. Note that because the MSD combines information about speed and directional persistence of the valuated cells, it can be considered a measure of the surface area explored by cells over time. Data are presented as mean ± SEM (control 1 [n = 60 cells], control 2 [n = 69 cells], control 3 [n = 82 cells], EBS-MD 1 [n = 76 cells], EBS-MD 2 [n = 76 cells], and EBS-MD 3 [n = 71 cells]). (**g**) Evaluation of the total velocities of control and EBS-MD fibroblasts over 356 min. Boxplots show the median, 25th percentiles, and 75th percentiles, whereas whiskers indicate the full range of data (from minimum to maximum). Each dot represents a single cell. $^{**}P < 0.01$, Kruskal–Wallis test with Dunn's posthoc test for multiple comparisons. (**h**) Heatmap illustrating the median velocities of control and EBS-MD fibroblasts as calculated for (**f**) over 365 min. The median velocity at each time point was assigned according to a color code ranging from 0 µm/min (dark purple) to 1 µm/min (light yellow) (control 1 [n = 60 cells], control 2 [n = 69 cells], control 3 [n = 82 cells], EBS-MD 1 [n = 76 cells], EBS-MD 2 [n = 76 cells], and EBS-MD 3 [n = 71 cells]). a.u., arbitrary unit; EBS-MD, epidermolysis bullosa simplex with muscular dystrophy; hr, hour; min, minute; MSD, mean square displacement.

healing functions, albeit drastically delayed. Because altered cell proliferation and/or apoptosis could contribute to the retarded wound-healing capacities of EBS-MD fibroblasts, we monitored cell growth over days (Supplementary Figure S7a) and/or performed an annexin V–detection assay to measure cell death (Supplementary Figure S7b), respectively. In these experiments, patient cells displayed slightly increased proliferation capacities and amounts of necrotic cells, whereas no alterations in the rate of apoptosis were observed.

Therefore, as a next step, we investigated the motility of single cells in more detail. EBS-MD and control fibroblasts were seeded in cell culture dishes for 4 hours, and individual

cells were followed over a period of 6 hours using time-lapse microscopy. Indeed, single-cell trajectories demonstrated that EBS-MD fibroblasts moved significantly less (Figure 5c), and accordingly, the median distance they traveled was considerably lower than that of control cells (Figure 5d). However, this was not caused by an increase in stopping and turning events because the directionality index (Gorelik and Gautreau, 2014) was comparable between both cell types (Figure 5e). Moreover, a reduced mean square displacement (Gorelik and Gautreau, 2014) indicated that EBS-MD fibroblasts explored smaller territories within the first 60 minutes of monitoring (Figure 5f); the total velocity over 6 hours was also significantly reduced (Figure 5g). To determine whether the observed impairments occur only within a certain period or during the whole time of the experiment, we plotted the velocity for each time point as a function of time (Figure 5h). Strikingly, whereas control cells showed a rather homogenous motion profile, EBS-MD fibroblasts presented a delayed kickoff, being almost immobile during the initial phase, and started to move after 100 minutes of measuring at reduced velocity.

Because fibroblast migration is fundamental for their ability to adapt upon mechanical perturbation, we exposed EBS-MD and control cells to cyclic, uniaxial stretch and measured their orientation (Kah et al., 2020). Although all cell types displayed a random orientation when no substrate stretch was applied, after 6 hours of continuous substrate stretch with a relative amplitude of 20%, control cells and fibroblasts from patient 3 with EBS-MD aligned themselves orthogonal to the direction of the stretching, whereas fibroblasts from patients 1 and 2 with EBS-MD seemed to retain a more random distribution (Supplementary Figure S8a–c), indicating that certain EBS-MD cells displayed compromised orientation upon exposure to mechanical strain.

Considering that the motility of EBS-MD fibroblasts was particularly impaired in the initial period after seeding, we hypothesized that they might have difficulties in adhering to the substrate. Even though fully (24 hours) spread fibroblasts did not show any significant difference in protein levels of the focal adhesion components talin or paxillin (Supplementary Figure S9a–c) and the subcellular localization of focal complexes as well as their numbers per cell remained comparable between both cell types (Supplementary Figure S9d and e), we determined the adhesion abilities of control and EBS-MD fibroblasts 4 hours after seeding. Cells were stained with phalloidin (Figure 6a) and classified according to their in vitro adhesion stage (Hong et al., 2006; Khalili and Ahmad, 2015) as attached, intermediate, or spread (Figure 6b). Strikingly, whereas 68% of control cells appeared fully spread after 4 hours, only 25% of EBS-MD fibroblasts belonged to that category, and almost 40% were just attached to their substrate (compared with 11% of control cells) (Figure 6c), indicating a dramatic decrease in the adhesion capacities of EBS-MD fibroblasts. Fluorescence staining of 4 hour–adhered cells using phalloidin or antibodies to vimentin demonstrated condensed actin and highly collapsed IF networks in patient cells, respectively (Supplementary Figure S10a). In addition, corresponding staining using anti-paxillin antibodies identified dramatic changes in the appearance of focal contacts in EBS-MD fibroblasts (Figure 6d). Even though the total number of focal adhesions remained unaltered in patient cells (Figure 6e), their length was significantly smaller than those of controls (Figure 6f). Likewise, significantly reduced spreading of murine *Plec*$^{-/-}$ cells 4 hours after seeding (Supplementary Figure S10b and c) confirmed that plectin deficiency in fibroblasts substantially derails their initial adhesion process.

DISCUSSION

Current research on plectinopathies is largely based on different animal models, including knockout or conditional mouse models as well as cells derived from them, which allowed fundamental insight into plectin's functional diversity and disease mechanism (Castañón and Wiche, 2021). However, evaluating the consequences of plectin deficiency in patient-derived cells is equally essential to understanding the disease, especially in the skin, where fundamental differences in wound-healing mechanisms and skin architecture between mouse and human hamper the pathological relevance of mouse experiments (Zomer and Trentin, 2018). To our knowledge, we performed in this study a previously never conducted, comprehensive analysis of skin fibroblasts derived from patients with EBS-MD and described the morphological and functional consequences of human *PLEC* loss-of-function alterations.

Development of EBS-MD has originally been attributed to a lack of plectin protein expression due to PTCs coupled with nonsense-mediated mRNA decay. Up to now, a total of 124 disease-causing *PLEC* variants have been published, predominantly loss-of-function alterations but also splice site variants, protein-truncating insertions/deletions, frameshift, nonsense, and missense variants (Kaneyasu et al., 2023; Vahidnezhad et al., 2022; Vishwanathan et al., 2022). In addition, the clinical manifestation of individual patients with plectinopathy varies considerably regarding the onset, progression, and disease manifestations, without a clear correlation to the location of the alterations in different domains (Vahidnezhad et al., 2022). Although our patients 1 and 2 with EBS-MD were reported with *PLEC* alterations inducing PTCs, patient 3 was heterozygous with a PTC-causing nonsense mutation and a 3-bp in-frame insertion (Bauer et al., 2001; Kunz et al., 2000; Natsuga et al., 2010a). In the latter variation, the insertion of an additional leucine into a stretch of four existing consecutive leucines has been shown to increase the hydrophobicity in the respective region, therefore inducing self-association of the mutant protein and its rapid degradation (Bauer et al., 2001). When we quantitatively addressed plectin mRNA content, levels of full-length and rodless transcripts were comparable between patient fibroblasts and control cells, indicating the presence of RNA messages with and without exon 31. Although our data are contradictory to those of previous semiquantitative assessments, revealing reduced levels of full-length plectin mRNA in the cells of patients with EBS-MD (Natsuga et al., 2010a), they are in line with the concept that nonsense-mediated mRNA decay, a post-translational process, detects and removes PTC-containing transcripts to prevail possibly deleterious effects (Inglis et al., 2023). Accordingly, when we evaluated protein levels, patients 1 and 2 with EBS-MD did not express any full-length plectin, whereas patient 3 with

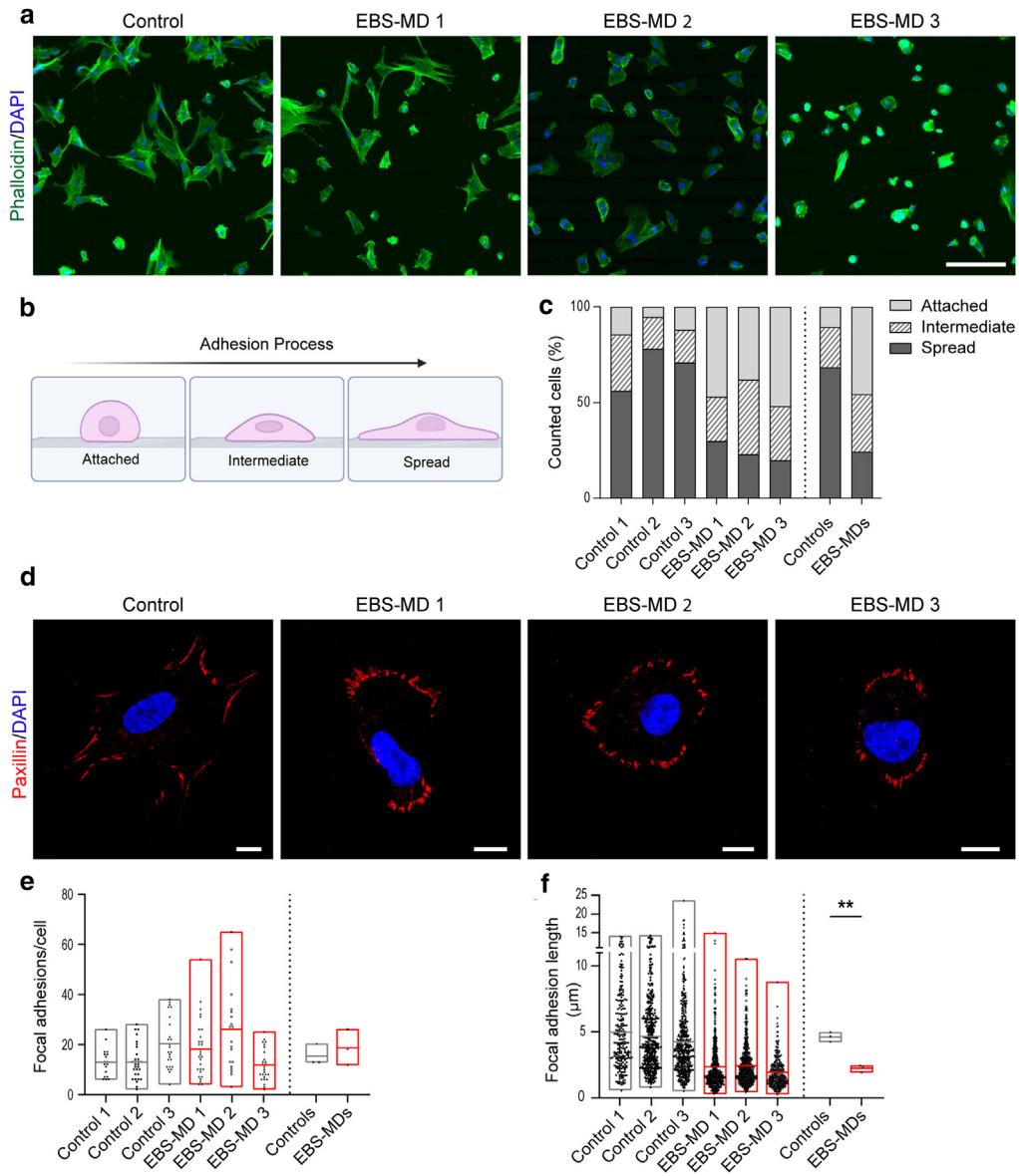

Figure 6. Impaired adhesion capacities of EBS-MD fibroblasts. (**a**) Overview pictures showing control and EBS-MD fibroblasts 4 h after seeding, stained for actin using phalloidin. Nuclei were visualized using DAPI. Bar = 150 µm. (**b**) Scheme illustrating the three categories that were used to classify adhered cells (Hong et al., 2006; Khalili and Ahmad, 2015). (**c**) Percentage of attached, intermediate, or spread cells after 4 h of adhesion (control 1 [n = 132 cells], control 2 [n = 110 cells], control 3 [n = 135 cells], EBS-MD 1 [n = 134 cells], EBS-MD 2 [n = 108 cells], and EBS-MD 3 [n = 103 cells]). (**d**) Control and EBS-MD fibroblasts 4 h after seeding were stained for paxillin. Nuclei were visualized using DAPI. Bar = 10 µm. (**e**) Numbers of focal adhesions per cell. Floating bar graphs show the mean and the full range of the data (from minimum to maximum). Each dot represents a single cell (control 1 [n = 18 cells], control 2 [n = 30 cells], control 3 [n = 25 cells], EBS-MD 1 [n = 29 cells], EBS-MD 2 [n = 20 cells], and EBS-MD 3 [n = 26 cells]). (**f**) Statistical evaluation of focal adhesion length. Floating bar graphs show the mean and the full range of the data (from minimum to maximum). Each dot represents one focal adhesion (control 1 [n = 231 focal adhesions, derived from 18 cells], control 2 [n = 386 focal adhesions, derived from 30 cells], control 3 [n = 505 focal adhesions, derived from 25 cells], EBS-MD 1 [n = 513 focal adhesions, derived from 29 cells], EBS-MD 2 [n = 521 focal adhesions, derived from 20 cells], and EBS-MD 3 [n = 305 focal adhesions, derived from 26 cells]). $^{**}P < 0.01$ compared with control cells; unpaired Student's *t*-test. EBS-MD, epidermolysis bullosa simplex with muscular dystrophy; h, hour.

EBS-MD displayed drastically reduced protein levels. Expression of rodless plectin versions, lacking the central rod domain owing to alternative splicing of exon 31 (Elliott et al., 1997), was observed in all cell lines analyzed, albeit in variable concentrations. Preserved expression of rodless plectin was suspected to prevent the more severe EBS associated with pyloric atresia and early demise (Natsuga et al., 2010a); however, a clear genotype–phenotype correlation remains to be demonstrated, and patients with EBS-MD without expression of rodless plectin protein have previously been published (Argente-Escrig et al., 2021; Gache et al., 1996; McLean et al., 1996; Winter et al., 2016). Together, our experiments demonstrated that full-length plectin, despite being expressed at the mRNA level, was completely lost on the protein level in the fibroblasts of patients 1 and 2 with EBS-MD and drastically reduced in the fibroblasts of patient 3 with EBS-MD. In addition, because no compensatory upregulation of rodless plectin was observed

in the cells of patients with EBS-MD, the overall low expression levels of plectin dictate the development of the disease.

Our results show that especially the vimentin IF network is drastically altered in EBS-MD fibroblasts, whereas actin filaments and microtubules remained largely unchanged. Increased lateral bundling of vimentin IFs and the formation of prominent ring-like structures around the nuclei, provoked by tightened bundling of the perinuclear vimentin IF cage (Lowery et al., 2015), was observed for all three patient cells. This was accompanied by increased areas completely devoid of vimentin between the filament bundles, leading to a considerable loss of network compactness. Similar to patient cells, the vimentin network of murine *Plec*$^{-/-}$ fibroblasts is not restricted to the central part of the cell but extends to the outermost boundary of the cell and displays increased bundling of filaments and the perinuclear vimentin cage (Burgstaller et al., 2010; Wiche and Winter, 2011). Because the latter observation could be specifically induced by siRNA knockdown of plectin in human control fibroblasts, it could be directly attributed to the loss of plectin protein. Our results are also in line with previous reports demonstrating increased bundling or even complete collapse of keratin or desmin IF networks in *Plec*$^{-/-}$ KCs or myoblasts, respectively (Osmanagic-Myers et al., 2006; Winter et al., 2014), indicating that a lack of plectin provokes increased bundling of any type of IF.

Moreover, we could solubilize increased amounts of vimentin from EBS-MD cell lysates. Our results are in line with previous studies, where different types of IFs, that is, keratin, vimentin, and desmin, turned out to be less stable and consequently more soluble upon extraction of murine KCs, fibroblasts, or myoblasts (Gregor et al., 2014; Osmanagic-Myers et al., 2006; Winter et al., 2014). Thus, in the absence of plectin-mediated linkage, IF networks lose their delicate order and become more vulnerable to various kinds of stress, leading to their disorganization and collapse (Wiche, 2021). In the case of vimentin, we could show that its increased solubility in EBS-MD fibroblasts cannot be ascribed to altered post-translational modifications such as site-specific phosphorylation, indicating that rather a lack of mechanical anchorage and/or altered dynamics leads to increased solubility in the patient cells. In summary, our experiments and those by others emphasize plectin's central role as a cytolinker of the IF architecture in various cell systems, including human dermal fibroblasts.

Previous studies convincingly demonstrated that plectin deficiency leads to major alterations of the mitochondrial morphology, including changes in shape and network organization in various murine cell types such as fibroblasts, myoblasts, or neurons (Valencia et al., 2021; Winter et al., 2015, 2008) as well as in muscle tissue derived from MCK-Cre/cKO (skeletal muscle-specific conditional plectin knockout) mice (Winter et al., 2015). Structural and/or functional alterations of mitochondria have also been described in skeletal muscle specimens from patients with EBS-MD, where succinate dehydrogenase and cytochrome c−oxidase stainings revealed fibers displaying abnormal pattern with coarse and thread-like organelle networks and fibers with rubbed-out lesions (Argente-Escrig et al., 2021; Bauer et al., 2001; Deev et al., 2017; Maselli et al., 2011; Schröder et al., 2002; Selcen et al., 2011; Walter et al., 2021; Winter et al., 2016; Yiu et al., 2011; Zrelski et al., 2021). Hence, the observed changes in the organelle morphology, that is, elongated mitochondrial networks in fibroblasts from patients with EBS-MD, significantly highlight a scenario in which mitochondrial pathology is a fundamental pathogenic mechanism that contributes to EBS-MD.

Moreover, assessing nuclear morphologies enabled us to gain further insights into additional organelle alterations in EBS-MD fibroblasts, such as the increased occurrence of deformed or blebbing nuclei, and structural alterations of the nuclear lamina (e.g., honeycomb structures or donut shapes) reminiscent of the nuclear alterations observed in nuclear lamina−related diseases (Stiekema et al., 2020; van Tienen et al., 2019). Analyzing the expression levels of nuclear protein, the effect of plectin deficiency was less obvious. Whereas LAP2α expression was drastically increased in patient 2 with EBS-MD and reduced in patient 3 with EBS-MD, similar protein levels were detected in the controls and in patient 1 with EBS-MD, indicating differential effects of the respective *PLEC* alterations, probably owing to genetic variations between human individuals. Contrarily, emerin protein levels were significantly reduced in lysates from all patients with EBS-MD as well as in murine *Plec*$^{-/-}$ fibroblasts, emphasizing a role of plectin in the emerin-mediated adaption to external forces (Guilluy et al., 2014). This hypothesis is also encouraged by a previous study in KCs, where disruption of the keratin cytoskeleton through loss of plectin facilitated increased nuclear deformation, which was attributed to the altered keratin filament density around the nucleus (Almeida et al., 2015). The authors of this study also described KCs displaying abnormal nuclear morphologies in the epidermis of patients with EBS-MD (Almeida et al., 2015). Moreover, plectin-dependent alterations in nuclear morphology have also been detected in myofibers obtained from MCK-Cre/cKO mice (Staszewska et al., 2015). Together, our data support the concept that plectin, likely by interacting with the nuclear envelope protein nesprin 3, connects the nucleus to IFs (Ketema et al., 2013; Wilhelmsen et al., 2005) and thereby protects the nucleus from mechanic deformation. Whether altered signaling pathways, such as YAP/TAZ signaling (Staszewska et al., 2015), might in addition to changed cellular mechanics contribute to the nuclear morphology of EBS-MD fibroblasts remains elusive. In any case, plectin-mediated IF networks are fundamental for mechanically connecting and integrating organelles, such as mitochondria or nuclei, within the cytoskeleton.

Dermal fibroblasts, the main cell type present in skin connective tissue, play an essential role during cutaneous wound healing. Our experiments showed that *PLEC* alterations significantly impaired the migration of EBS-MD fibroblasts as well as their initial adhesion to the substratum. Especially within the first hours after seeding, EBS-MD fibroblasts hardly migrated, and at a later stage and/or upon mechanical stretching, migration was hampered. The delayed kickoff of patient cells could be attributed on one hand to reduced adhesion capability and morphological alterations of their focal adhesion contacts, which were significantly smaller than those of control fibroblasts. In addition, we

found both the actin and the vimentin IF networks to be highly collapsed in the patients' cells after 4 hours of adhesion, even though stationary control and EBS-MD fibroblasts displayed similar actin organization. These experiments support the notion that both cytoskeletal systems play a substantial role in the cellular adhesion process. Whether this concerted action is directly mediated through plectin or indirectly through plectin-related processes remains to be investigated. However, a physical interaction between vimentin IFs and F-actin bundles as mediated by plectin has been demonstrated by high-resolution immunoelectron microscopic methods (Svitkina et al., 1996), and the importance of vimentin–actin interactions has recently been corroborated by structured illumination microscopy in combination with cryoelectron tomography (Wu et al., 2022). Accordingly, in previous experiments, murine fibroblasts deficient in either protein, plectin, or vimentin were found compromised in their migration abilities (Andrä et al., 1998; Eckes et al., 1998). When the dynamics of vimentin IF networks were monitored in spreading mouse fibroblasts, plectin was associated with vimentin already in the early stages of filament assembly and recruited motile vimentin intermediates to mature focal adhesions (Burgstaller et al., 2010; Spurny et al., 2008). Thereby, focal adhesions functioned as anchorage sites for vimentin IFs, with plectin as a cytolinker forming a connection that is a prerequisite for efficient integrin-mediated mechanotransduction (Gregor et al., 2014). Plectin's significance for migratory abilities is further highlighted in recent studies addressing its role as a protumorigenic regulator of cancer cell invasion and metastasis (Perez et al., 2021a, 2021b). For instance, in hepatocellular carcinoma cells, plectin expression was significantly increased compared with that in normal liver cells, and downregulation of plectin drastically reduced the migration abilities of hepatocellular carcinoma cells (Xu et al., 2022).

In summary, our experiments showed that *PLEC* alterations in human fibroblasts, although leaving actin and microtubule networks largely unaltered, significantly impaired vimentin IFs, thereby leading to increased filament bundling and the formation of nuclei-encasing ring-like structures. In addition, EBS-MD fibroblasts displayed drastically altered mitochondrial and nuclear morphologies compared with control cells. A reduced overall motility, with an even more pronounced dysfunction in the initial phase after seeding of cells, and weakened adhesion capacities indicated that essential fibroblast functions are significantly hampered in EBS-MD cells (Figure 7). However, cell biological analyses of rare diseases are generally hampered by the scarce availability of human tissue specimens and cells derived thereof. Accordingly, our study was limited by the small sample size of having fibroblasts derived from only three different patients with EBS-MD, and we cannot exclude that some morphological and/or functional alterations observed in our EBS-MD fibroblasts originated from interdonor variability rather than from the different *PLEC* alterations. To overcome these experimental limitations and to investigate whether the virtual lack of full-length plectin protein was the underlying cause of vimentin bundling and nuclear ring formation, we complemented our study by evaluating IF networks in siRNA-mediated plectin-depleted human control fibroblasts and murine *Plec*$^{-/-}$ fibroblasts. Likewise, the finding of deformed nuclear morphologies and reduced emerin protein levels in cells from patients with EBS-MD as well as in *Plec*$^{-/-}$ fibroblasts opens a perspective for possible functions, but more in-depth studies will be needed to address these questions. Finally, similar to adhesion capacities in EBS-MD fibroblasts, impaired adhesion capacities in *Plec*$^{-/-}$ fibroblasts as well as previously reported elongated mitochondria and impaired migration abilities (Andrä et al., 1998; Winter et al., 2008) indicated that the lack/drastic reduction of full-length plectin protein is the underlying mechanism of the observed alterations. Our findings not only open up additional insights into the role of plectin in human dermal fibroblasts but also provide a basis for an increased understanding of EBS-MD–associated disease mechanisms.

MATERIALS AND METHODS

Cell culture

Primary human dermal fibroblasts from controls and patients 1 and 2 with EBS-MD were prepared after informed written patient consent. The project was approved by the ethics committee of the University of Freiburg (Freiburg, Germany) (ethics number 293-14) and was conducted according to the Declaration of Helsinki principles. Immortalized fibroblasts from patient 3 EBS-MD were kindly

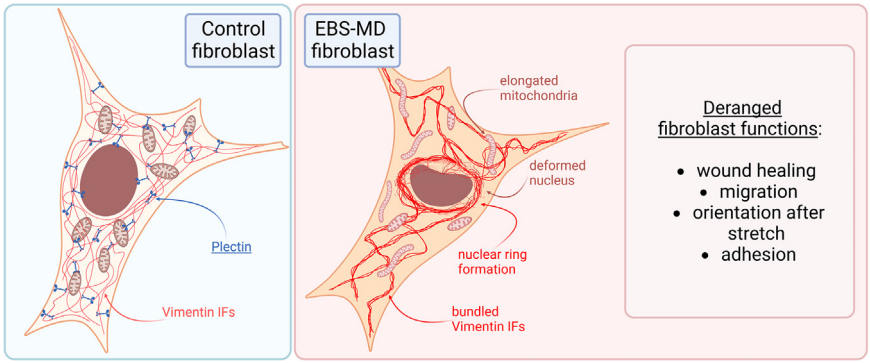

Figure 7. Model depicting the downstream effects of *PLEC* alterations in fibroblasts. Illustrative scheme summarizing the morphological and functional alterations observed in patient fibroblasts compared with those in control cells. Altered cytoarchitecture in EBS-MD fibroblasts includes massive bundling of vimentin IF networks and the occurrence of ring-like nuclei-encasing filament bundles, elongated mitochondrial networks, and deformed nuclear morphologies. In addition, *PLEC* alterations impaired wound healing and migration abilities, orientation after cyclic stretch, and adhesion. EBS-MD, epidermolysis bullosa simplex with muscular dystrophy; IF, intermediate filament.

provided by the EB House Salzburg and originally published by Wally et al. (2008). Primary control cells and cells from patients with EBS-MD were used at passages 7–15 in all experiments, whereas the cell line from patient 3 with EBS-MD was used at passages 10–19. Immortalized murine fibroblasts were derived from plectin wild-type (*Plec*$^{+/+}$) and plectin-deficient (*Plec*$^{-/-}$) p53-deficient (*p53*$^{-/-}$) mice as described previously (Andrä et al., 2003) and used at passage numbers 20–30. Cells were cultivated in DMEM (Gibco, Billings, MT) supplemented with 10% fetal calf serum (Sigma-Aldrich, St. Louis, MO), 2 mM L-glutamine (Gibco), 50 U/ml penicillin, and 50 μg/ml streptomycin (Gibco) at 37 °C and 5% carbon dioxide.

Transient knockdown of plectin was performed in control fibroblasts as previously described (Cheng et al., 2015). In brief, cells were seeded onto glass coverslips and transfected with four siRNAs targeting the human plectin mRNA (ON-TARGETplus SMARTPool, GE Healthcare Dharmacon, Lafayette, CO) using Lipofectamine RNAiMAX (Thermo Fisher Scientific, Waltham, MA) according to the manufacturer's instructions for 48 hours. Transfected cells were fixed and processed for immunofluorescence microscopy as described below. Scramble siRNA–transfected cells were used as controls.

Analysis of cell morphology, proliferation, and apoptosis

For morphometric analysis, transmitted-light microscopic pictures were obtained with an optocam-1 camera mounted to a Nikon eclipse TS100 microscope (×20 magnification). Cell contours of fibroblasts were measured, and mean cell area, perimeter, shape factor, and aspect ratio were analyzed using ImageJ software (National Institutes of Health, Bethesda, MD). The proliferation and apoptosis assays have been performed as described (Spörrer et al., 2019).

RNA isolation and RT-qPCR

Total RNA was isolated using the RNeasy Mini kit (Qiagen, Hilden, Germany) according to the manufacturers' instructions. For cDNA synthesis, RNA (130 ng) was reversely transcribed using superscript IV reverse transcriptase (Thermo Fisher Scientific), and real-time PCR was performed using the SensiMix HI-ROX kit (Bioline, London, United Kingdom) and a CFX96 Touch System (Bio-Rad Laboratories, Hercules, CA). Primer sequences are listed in Supplementary Table S3. Relative gene expression levels were determined according to a modified $2^{-\Delta\Delta CT}$ equation, and normalization was performed against a common calibrator calculated from respective values obtained from three control fibroblasts (Hellemans et al., 2007; Vandesompele et al., 2002). *TBP* and *RPLP0* were used as internal reference genes.

Preparation of cell lysates, SDS-PAGE, and immunoblotting analysis

Cells were washed with PBS and directly scraped off in 6× SDS sample buffer (500 mM Tris-hydrogen chloride, pH 6.8, 600 mM dichlorodiphenyltrichloroethane, 10% SDS, 0.1% bromphenol-blue, 30% glycerol), DNA sheared by pressing the samples through a 27 gauge needle, boiled for 5 minutes at 95 °C, and stored at −20 °C (Winter et al., 2014). SDS-PAGE was performed according to Laemmli (1970). Proteins were transferred to nitrocellulose membranes (Protran 0.2 NC, Amersham Bioscience, Amersham, United Kingdom) using a Mini PROTEAN Tetra Cell blot apparatus (Bio-Rad Laboratories). Membranes were scanned, and the amounts of protein contained in individual bands were quantified using ImageJ software. For evaluation of protein expression levels, cell lysates were obtained at two different time points/passage numbers, and immunoblotting experiments were performed in duplicates or triplicates.

Antibodies

For immunofluorescence microscopy and immunoblotting, the following primary antibodies were used: rabbit antiserum (AS) to GAPDH (G9545, Sigma-Aldrich); guinea pig AS to plectin (GP21, Progen Biotechnic, Heidelberg, Germany); mouse mAbs to tubulin (B512, Sigma-Aldrich); rat mAbs to tubulin (YL1/2, Origene, Rockville, MD); mouse mAbs to actin (AC-40, Sigma-Aldrich); chicken AS to vimentin (NB300-223, Novus Biologicals, Littleton, CO); goat AS to vimentin (P. Traub, University of Bonn, Bonn, Germany); mouse mAbs to talin (84D, Sigma-Aldrich); mouse mAbs to paxillin (5H11, Invitrogen, Waltham, MA); mouse mAbs to lamin A/C (sc-376248 E-1, Santa Cruz Biotechnology, Dallas, TX); rabbit AS to LAP2α (Vlcek et al., 1999); mouse mAbs to emerin (MANEM15[8E1], Developmental Studies Hybridoma Bank, Iowa City, IA); and the oxidative phosphorylation antibody cocktail detecting ATP5A, UQCRC2, SDHB, COXII, and NDUFB8 subunits (45-8199, Invitrogen). For immunofluorescence microscopy, primary antibodies were used in combination with biotinylated goat anti-guinea pig IgG, together with streptavidin-conjugated Alexa Plus 488, goat anti-rat IgG Alexa Fluor Plus 555, donkey anti-goat IgG Alexa Fluor Plus 555, donkey anti-rabbit IgG Alexa Fluor Plus 555, and donkey anti-mouse IgG Alexa Plus 555 (all from Invitrogen). For immunoblot analyses, horseradish peroxidase–conjugated secondary antibodies from Jackson ImmunoResearch (West Grove, PA) (rabbit, mouse) or Invitrogen (guinea pig, chicken) in combination with the SuperSignal West Pico PLUS ECL detection kit (Thermo Fisher Scientific) were used.

Immunofluorescence microscopy

Cells were either fixed with ice-cold methanol for 90 seconds at −20 °C or with 3.7% paraformaldehyde for 10 minutes at room temperature, followed by 10-minute permeabilization with 0.05% Triton X-100, and immune-stained as described (Winter et al., 2008). F-actin was visualized with phalloidin-Atto 488 (Sigma-Aldrich), and nuclei were visualized with DAPI (Sigma-Aldrich) or DRAQ5 (Invitrogen). Microscopy was performed using an Olympus FLUOVIEW FV3000 confocal microscope equipped with PlanApo N 60× 1.4 numerical aperture and UPLAN FLN 40× 1.3 numerical aperture objective lenses (Olympus, Tokyo, Japan). Z-stacks were recorded using the Olympus FluoView software and processed with ImageJ software to generate maximum intensity projections unless stated otherwise.

For assessing vimentin distributions, fluorescence intensity plots were generated using the ImageJ Plot Profile function. Mitochondrial morphologies were classified as (i) fragmented, comprising individual round- or rod-shaped organelles, >80% displaying an axial length <5 μm; (ii) intermediate, with the majority of mitochondria ~5 μm; or (iii) elongated, comprising interconnected mitochondria in branched networks, >80% displaying a length >5 μm as described (Winter et al., 2008). Nuclei were categorized as (i) normal; (ii) irregularly shaped, indicating nuclei that display deviations from the typical oval or spherical shape; or (iii) blebbing nuclei with severe structural alterations such as nuclear blebs, constrictions, or incisions (Lammerding et al., 2005).

Proteomic analysis

Washed cells, lysed in a high-urea buffer, were used for proteomics analyses (Herzog et al., 2020). For the bottom-up approach, 50 μg protein per sample was digested (trypsin/LysC), reduced, and alkylated using SP3-beads and prepared for analysis, as described before (Daniel-Fischer et al., 2022). Samples were analyzed by liquid

chromatography–mass spectrometry on an Ultimate 3000 RSLC nano coupled directly to an Exploris 480 with FAIMS Pro interface (all from Thermo Fisher Scientific), with settings and analysis parameters as described before. Data were analyzed using ProteomeDiscoverer (version 2.4.0.305, Thermo Fisher Scientific) with SequestHT as a search engine (*Homo sapiens* [SwissProt]; maximum missed cleavage sites of 2; static modifications: carbamidomethyl [C]; dynamic modifications: oxidation [M], phosphor [S, T, Y], acetyl [N-terminus], met-loss [M], met-loss + acetyl [M]; precursor mass tolerance: 10 ppm; fragment mass tolerance: 0.02 Da). For the top-down approach, 70 μg protein per sample was separated for the first dimension by isoelectric focusing and per molecular weight for the second dimension by SDS-PAGE. After total protein detection with the stain-free method, semidry blotting onto polyvinylidene fluoride membranes was performed as described before (Herzog et al., 2020). Antibody-based detection was performed as described earlier. Image overlay and analysis were performed using Delta2D (version 4.8.0; DECODON GmbH, Greifswald, Germany) with the previously described algorithm.

Fractionation of soluble and insoluble vimentin proteins

Fibroblasts were harvested in a high salt detergent-containing buffer containing 0.5% Triton X-100, 100 mM sodium chloride, 50 mM 4-(2-hydroxyethyl)-1-piperazineethanesulfonic acid, pH 7.0, 5 mM magnesium chloride, 0.1 mM dichlorodiphenyltrichloroethane, 1 mM EGTA, 2 mM phenylmethylsulfonyl fluoride, 10 mM β-glycerophosphate, 50 mM sodium fluoride, 1 mM sodium orthovanadate, and complete Mini Protease Inhibitor Cocktail (Roche, Basel Switzerland); homogenized using a Dounce tissue grinder (Wheaton); and incubated for 45 minutes at 4 °C with end-over-end rotation. After centrifugation for 30 minutes at 15,800*g* and 4 °C, the soluble supernatant was collected, and the insoluble pellet was dissolved in 8 M urea by end-over-end rotation for 30 minutes at 4 °C. Soluble and insoluble fractions were separated by SDS-PAGE.

Cell motility and adhesion assays

Fibroblast motility measurements were made by scratching a confluent culture dish with a sterile 200 μl pipette tip. The in vitro migration assay has been performed as described (Spörrer et al., 2019). The pictures were analyzed with ImageJ.

For assessing single-cell motility, 1×10^5 cells per well were seeded in six-well plates (Thermo Fisher Scientific) and allowed to attach for 4 hours. Images were obtained with a motorized Zeiss Axio Observer 7 inverted microscope equipped with an Axiocam 208c camera, an environmental chamber (37 °C, 5% carbon dioxide), and an EC Plan-Neofluor 10× objective every 4 minutes over a time period of 6 hours. Subject trajectories of cells were analyzed using the ImageJ Manual Tracking plugin. Flower plots, directionality index, and mean square displacement were calculated with DiPer (Gorelik and Gautreau, 2014).

Adhesion properties were determined by seeding 4×10^4 cells on Ø 13 mm glass coverslips. After 4-hour incubation at 37 °C and 5% carbon dioxide, cells were fixed and stained for F-actin, vimentin, and nuclei. Overview images were obtained with an Olympus VS-BX slide scanner equipped with a UPLSAPO 0 ×100 1.4NA objective lens (Olympus). For quantification, cells were assigned into three different groups according to their adhesion status (Hong et al., 2006; Khalili and Ahmad, 2015) (see also Figure 5d): (i) attached, where round cells just sedimented to their substrate; (ii) intermediate, where cells flatten and start to spread their cell bodies; and (iii) fully spread and stably adhered cells.

Cell stretching

Stretching experiments were performed using a custom-made stretcher device (Kah et al., 2020). A total of 2.5×10^4 cells were seeded on flexible polydimethylsiloxane (Sylgard 184) membranes with 4 cm^2 internal surface (coated with 5 μg/ml fibronectin) and incubated under standard cell culture conditions for 24 hours. Samples were mounted on a stepper-motor-driven, uniaxial cell stretcher device and exposed to cyclic stretch at 20% amplitude and a frequency of 0.1 Hz for 6 hours. To quantify the orientation of control and EBS-MD fibroblasts in response to cyclic, uniaxial stretch, cells were fixed and stained for vimentin as described earlier. Z-stacks were obtained using a Leica SP5X confocal microscope and processed with ImageJ software to generate maximum-intensity projections. An ellipsis was fit around each cell, and the angle θ between the semimajor axis and the stretching direction was determined, with $\cos(2\theta)$ being a measure of cell orientation. This way, cells that orientated in parallel to the stretching direction result in $\cos(2\theta) = 1$, whereas cells that orientated orthogonal to the stretching direction result in $\cos(2\theta) = -1$, and the average value of $\cos(2\theta)$ for a population of randomly orientated cells is 0.

Statistical analysis

Data analyses and statistical evaluations were performed using Excel or GraphPad Prism software. The number of experiments is indicated in the figure legends; data are presented as mean ± SEM or median with minimum and maximum (whiskers). Comparisons between values of two groups were made using an unpaired, two-tailed Student's *t*-test ($\alpha = 0.05$) or Kruskal–Wallis test ($\alpha = 0.05$) with Dunn's posthoc test for multiple comparisons. A $P < 0.05$ was considered statistically significant. Final assembly and preparation of figures were performed with Adobe Illustrator CS2.

Data availability statement

No large datasets were generated or analyzed during this study.

ORCIDs

Michaela M. Zrelski: https://orcid.org/0000-0003-4305-2292
Sabrina Hösele: https://orcid.org/0000-0002-5976-1328
Monika Kustermann: https://orcid.org/0000-0003-0208-1636
Petra Fichtinger: https://orcid.org/0000-0002-9239-1111
Delf Kah: https://orcid.org/0000-0002-3800-2461
Ioannis Athanasiou: https://orcid.org/0000-0002-5158-673X
Philipp R. Esser: https://orcid.org/0000-0002-7379-9699
Anja Wagner: https://orcid.org/0009-0008-7853-1780
Rebecca Herzog: https://orcid.org/0000-0003-1946-7770
Klaus Kratochwill: https://orcid.org/0000-0003-0803-614X
Wolfgang H. Goldmann: https://orcid.org/0000-0003-0738-2665
Dimitra Kiritsi: https://orcid.org/0000-0002-2331-8981
Lilli Winter: https://orcid.org/0000-0002-6368-1160

CONFLICT OF INTEREST

The authors state no conflict of interest.

ACKNOWLEDGMENTS

The authors would like to thank the EB House Austria (Salzburg, Austria) for kindly providing immortalized fibroblasts from patients with epidermolysis bullosa simplex with muscular dystrophy; Gerhard Wiche for kindly providing immortalized murine fibroblasts; Roland Foisner for kindly providing antibodies for LAP2α, lamin A/C, and emerin; and Sascha Martens for kindly donating scrambled small interfering RNA. Graphical abstract and Figures 1a, 6b, and 7 and Supplementary Figure 8b were prepared with BioRender. This work was supported by the Austrian Science Research Fund grants P31541-B27 and I6049-B to LW, Marie Sklodowska-Curie Action, Innovative Training Networks, EU grant agreement number 812772 to WHG, and Deutsche Forschungsgemeinschaft (German Research Foundation) project 383071714 (grant FA-336/12.1) to DK (DKa). DKa is funded by the Deutsche Forschungsgemeinschaft through SFB1160 projects B03, SFB-1479 – project identification: 441891347, and KI1795/2-1. The financial support of the Austrian Federal Ministry of Science, Research and Economy

and the National Foundation for Research, Technology and Development to KK is gratefully acknowledged.

AUTHOR CONTRIBUTIONS

Conceptualization: MMZ, DKi, LW; Data Curation: MMZ, LW; Funding Acquisition: WHG, DKa, DKi, LW; Methodology: MMZ, MK, DKa, RH, KK, WHG, DKi, LW; Investigation: MMZ, SH, MK, PF, IA, PRE, DKa, AW; Supervision: WHG, DKi, LW; Project administration: LW; Writing – Original Draft Preparation: MMZ, LW; Writing – Review and Editing: MMZ, WHG, DKi, LW

SUPPLEMENTARY MATERIAL

Supplementary material is linked to the online version of the paper at www.jidonline.org, and at https://doi.org/10.1016/j.jid.2023.08.020.

REFERENCES

Almeida FV, Walko G, McMillan JR, McGrath JA, Wiche G, Barber AH, et al. The cytolinker plectin regulates nuclear mechanotransduction in keratinocytes. J Cell Sci 2015;128:4475–86.

Amiri N, Golin AP, Jalili RB, Ghahary A. Roles of cutaneous cell-cell communication in wound healing outcome: an emphasis on keratinocyte-fibroblast crosstalk. Exp Dermatol 2022;31:475–84.

Andrä K, Kornacker I, Jörgl A, Zörer M, Spazierer D, Fuchs P, et al. Plectin-isoform-specific rescue of hemidesmosomal defects in plectin (-/-) keratinocytes. J Invest Dermatol 2003;120:189–97.

Andrä K, Nikolic B, Stöcher M, Drenckhahn D, Wiche G. Not just scaffolding: plectin regulates actin dynamics in cultured cells. Genes Dev 1998;12:3442–51.

Argente-Escrig H, Schultheis D, Kamm L, Schowalter M, Thiel C, Türk M, et al. Plectin-related scapuloperoneal myopathy with treatment-responsive myasthenic syndrome. Neuropathol Appl Neurobiol 2021;47:352–6.

Bauer JW, Rouan F, Kofler B, Rezniczek GA, Kornacker I, Muss W, et al. A compound heterozygous one amino-acid insertion/nonsense mutation in the plectin gene causes epidermolysis bullosa simplex with plectin deficiency. Am J Pathol 2001;158:617–25.

Burgstaller G, Gregor M, Winter L, Wiche G. Keeping the vimentin network under control: cell-matrix adhesion-associated plectin 1f affects cell shape and polarity of fibroblasts. Mol Biol Cell 2010;21:3362–75.

Castañón MJ, Walko G, Winter L, Wiche G. Plectin-intermediate filament partnership in skin, skeletal muscle, and peripheral nerve. Histochem Cell Biol 2013;140:33–53.

Castañón MJ, Wiche G. Identifying plectin isoform functions through animal models. Cells 2021;10:2453.

Chavanas S, Pulkkinen L, Gache Y, Smith FJ, McLean WH, Uitto J, et al. A homozygous nonsense mutation in the PLEC1 gene in patients with epidermolysis bullosa simplex with muscular dystrophy. J Clin Invest 1996;98:2196–200.

Cheng CC, Lai YC, Lai YS, Hsu YH, Chao WT, Sia KC, et al. Transient knockdown-mediated deficiency in plectin alters hepatocellular motility in association with activated FAK and Rac1-GTPase. Cancer Cell Int 2015;15:29.

Daniel-Fischer L, Sobieszek IJ, Wagner A, Sacnun JM, Watschinger B, Aufricht C, et al. In-depth analysis of the extracorporeal proteome adsorbed to dialysis membranes during hemodialysis. Membranes (Basel) 2022;12:1120.

Deev RV, Bardakov SN, Mavlikeev MO, Yakovlev IA, Umakhanova ZR, Akhmedova PG, et al. Glu20Ter Variant in PLEC 1f isoform Causes Limb-Girdle Muscle Dystrophy with Lung Injury. Front Neurol 2017;8:367.

Eckes B, Dogic D, Colucci-Guyon E, Wang N, Maniotis A, Ingber D, et al. Impaired mechanical stability, migration and contractile capacity in vimentin-deficient fibroblasts. J Cell Sci 1998;111:1897–907.

Elliott CE, Becker B, Oehler S, Castañón MJ, Hauptmann R, Wiche G. Plectin transcript diversity: identification and tissue distribution of variants with distinct first coding exons and rodless isoforms. Genomics 1997;42:115–25.

Foisner R, Wiche G. Structure and hydrodynamic properties of plectin molecules. J Mol Biol 1987;198:515–31.

Fuchs P, Zörer M, Rezniczek GA, Spazierer D, Oehler S, Castañón MJ, et al. Unusual 5′ transcript complexity of plectin isoforms: novel tissue-specific exons modulate actin binding activity. Hum Mol Genet 1999;8:2461–72.

Gache Y, Chavanas S, Lacour JP, Wiche G, Owaribe K, Meneguzzi G, et al. Defective expression of plectin/HD1 in epidermolysis bullosa simplex with muscular dystrophy. J Clin Invest 1996;97:2289–98.

Gorelik R, Gautreau A. Quantitative and unbiased analysis of directional persistence in cell migration. Nat Protoc 2014;9:1931–43.

Gostyńska KB, Lemmink H, Bremer J, Pas HH, Nijenhuis M, van den Akker PC, et al. A PLEC isoform identified in skin, muscle, and heart. J Invest Dermatol 2017;137:518–22.

Gostyńska KB, Nijenhuis M, Lemmink H, Pas HH, Pasmooij AM, Lang KK, et al. Mutation in exon 1a of PLEC, leading to disruption of plectin isoform 1a, causes autosomal-recessive skin-only epidermolysis bullosa simplex. Hum Mol Genet 2015;24:3155–62.

Gregor M, Osmanagic-Myers S, Burgstaller G, Wolfram M, Fischer I, Walko G, et al. Mechanosensing through focal adhesion-anchored intermediate filaments. FASEB J 2014;28:715–29.

Guilluy C, Osborne LD, Van Landeghem L, Sharek L, Superfine R, Garcia-Mata R, et al. Isolated nuclei adapt to force and reveal a mechanotransduction pathway in the nucleus. Nat Cell Biol 2014;16:376–81.

Has C, Bauer JW, Bodemer C, Bolling MC, Bruckner-Tuderman L, Diem A, et al. Consensus reclassification of inherited epidermolysis bullosa and other disorders with skin fragility. Br J Dermatol 2020;183:614–27.

Hellemans J, Mortier G, De Paepe A, Speleman F, Vandesompele J. qBase relative quantification framework and software for management and automated analysis of real-time quantitative PCR data. Genome Biol 2007;8:R19.

Herzog R, Wagner A, Wrettos G, Stampf K, Bromberger S, Sperl E, et al. Improved alignment and quantification of protein signals in two-dimensional Western blotting. J Proteome Res 2020;19:2379–90.

Hong S, Ergezen E, Lec R, Barbee KA. Real-time analysis of cell-surface adhesive interactions using thickness shear mode resonator. Biomaterials 2006;27:5813–20.

Inglis AJ, Guna A, Gálvez-Merchan Á Pal A, Esantsi TK, Keys HR, et al. Coupled protein quality control during nonsense-mediated mRNA decay. J Cell Sci 2023;136:cs261216.

Kah D, Winterl A, Přechová M, Schöler U, Schneider W, Friedrich O, et al. A low-cost uniaxial cell stretcher for six parallel wells. HardwareX 2020;9:e00162.

Kaneyasu H, Takahashi K, Ohta N, Okada S, Kimura S, Yasuno S, et al. Novel compound heterozygous mutations in the PLEC gene in a neonate with epidermolysis bullosa simplex with pyloric atresia. J Dermatol 2023;50:239–44.

Ketema M, Kreft M, Secades P, Janssen H, Sonnenberg A. Nesprin-3 connects plectin and vimentin to the nuclear envelope of Sertoli cells but is not required for Sertoli cell function in spermatogenesis. Mol Biol Cell 2013;24:2454–66.

Khalili AA, Ahmad MR. A review of cell adhesion studies for biomedical and biological applications. Int J Mol Sci 2015;16:18149–84.

Kiritsi D, Tsakiris L, Schauer F. Plectin in skin fragility disorders. Cells 2021;10:2738.

Koss-Harnes D, Høyheim B, Jonkman MF, de Groot WP, de Weerdt CJ, Nikolic B, et al. Life-long course and molecular characterization of the original Dutch family with epidermolysis bullosa simplex with muscular dystrophy due to a homozygous novel plectin point mutation. Acta Derm Venereol 2004;84:124–31.

Koster J, Borradori L, Sonnenberg A. Hemidesmosomes: molecular organization and their importance for cell adhesion and disease. Handb Exp Pharmacol 2004;165:243–80.

Kunz M, Rouan F, Pulkkinen L, Hamm H, Jeschke R, Bruckner-Tuderman L, et al. Mutation reports: epidermolysis bullosa simplex associated with severe mucous membrane involvement and novel mutations in the plectin gene. J Invest Dermatol 2000;114:376–80.

Kyrova J, Kopeckova L, Buckova H, Mrazova L, Vesely K, Hermanova M, et al. Epidermolysis bullosa simplex with muscular dystrophy. Review of the literature and a case report. J Dermatol Case Rep 2016;10:39–48.

Laemmli UK. Cleavage of structural proteins during the assembly of the head of bacteriophage T4. Nature 1970;227:680–5.

Lammerding J, Hsiao J, Schulze PC, Kozlov S, Stewart CL, Lee RT. Abnormal nuclear shape and impaired mechanotransduction in emerin-deficient cells. J Cell Biol 2005;170:781–91.

Liu CG, Maercker C, Castañón MJ, Hauptmann R, Wiche G. Human plectin: organization of the gene, sequence analysis, and chromosome localization (8q24). Proc Natl Acad Sci USA 1996;93:4278–83.

Lowery J, Kuczmarski ER, Herrmann H, Goldman RD. Intermediate filaments play a pivotal role in regulating cell architecture and function. J Biol Chem 2015;290:17145–53.

Martínez-Santamaría L, Maseda R, de Arriba MDC, Membrilla JA, Sigüenza AI, Mascías J, et al. Evaluation of systemic gentamicin as translational readthrough therapy for a patient with epidermolysis bullosa simplex with muscular dystrophy owing to PLEC1 pathogenic nonsense variants. JAMA Dermatol 2022;158:439–43.

Maselli RA, Arredondo J, Cagney O, Mozaffar T, Skinner S, Yousif S, et al. Congenital myasthenic syndrome associated with epidermolysis bullosa caused by homozygous mutations in PLEC1 and CHRNE. Clin Genet 2011;80:444–51.

McLean WH, Pulkkinen L, Smith FJ, Rugg EL, Lane EB, Bullrich F, et al. Loss of plectin causes epidermolysis bullosa with muscular dystrophy: cDNA cloning and genomic organization. Genes Dev 1996;10:1724–35.

Nakamura H, Natsuga K, Nishie W, McMillan JR, Nakamura H, Sawamura D, et al. DNA-based prenatal diagnosis of plectin-deficient epidermolysis bullosa simplex associated with pyloric atresia. Int J Dermatol 2011;50:439–42.

Natsuga K, Nishie W, Akiyama M, Nakamura H, Shinkuma S, McMillan JR, et al. Plectin expression patterns determine two distinct subtypes of epidermolysis bullosa simplex. Hum Mutat 2010a;31:308–16.

Natsuga K, Nishie W, Nishimura M, Shinkuma S, Watanabe M, Izumi K, et al. Loss of interaction between plectin and type XVII collagen results in epidermolysis bullosa simplex. Hum Mutat 2017;38:1666–70.

Natsuga K, Nishie W, Shinkuma S, Arita K, Nakamura H, Ohyama M, et al. Plectin deficiency leads to both muscular dystrophy and pyloric atresia in epidermolysis bullosa simplex. Hum Mutat 2010b;31:E1687–98.

Osmanagic-Myers S, Gregor M, Walko G, Burgstaller G, Reipert S, Wiche G. Plectin-controlled keratin cytoarchitecture affects MAP kinases involved in cellular stress response and migration. J Cell Biol 2006;174:557–68.

Perez SM, Brinton LT, Kelly KA. Plectin in cancer: from biomarker to therapeutic target. Cells 2021:10.

Perez SM, Dimastromatteo J, Landen CN Jr, Kelly KA. A novel monoclonal antibody targeting cancer-specific plectin has potent antitumor activity in ovarian cancer. Cells 2021b;10:2218.

Rezniczek GA, Abrahamsberg C, Fuchs P, Spazierer D, Wiche G. Plectin 5′-transcript diversity: short alternative sequences determine stability of gene products, initiation of translation and subcellular localization of isoforms. Hum Mol Genet 2003;12:3181–94.

Schröder R, Kunz WS, Rouan F, Pfendner E, Tolksdorf K, Kappes-Horn K, et al. Disorganization of the desmin cytoskeleton and mitochondrial dysfunction in plectin-related epidermolysis bullosa simplex with muscular dystrophy. J Neuropathol Exp Neurol 2002;61:520–30.

Selcen D, Juel VC, Hobson-Webb LD, Smith EC, Stickler DE, Bite AV, et al. Myasthenic syndrome caused by plectinopathy. Neurology 2011;76:327–36.

Spörrer M, Prochnicki A, Tölle RC, Nyström A, Esser PR, Homberg M, et al. Treatment of keratinocytes with 4-phenylbutyrate in epidermolysis bullosa: lessons for therapies in keratin disorders. EBiomedicine 2019;44:502–15.

Spurny R, Gregor M, Castañón MJ, Wiche G. Plectin deficiency affects precursor formation and dynamics of vimentin networks. Exp Cell Res 2008;314:3570–80.

Staszewska I, Fischer I, Wiche G. Plectin isoform 1-dependent nuclear docking of desmin networks affects myonuclear architecture and expression of mechanotransducers. Hum Mol Genet 2015;24:7373–89.

Stiekema M, van Zandvoort MAMJ, Ramaekers FCS, Broers JLV. Structural and mechanical aberrations of the nuclear lamina in disease. Cells 2020;9:1884.

Svitkina TM, Verkhovsky AB, Borisy GG. Plectin sidearms mediate interaction of intermediate filaments with microtubules and other components of the cytoskeleton. J Cell Biol 1996;135:991–1007.

Vahidnezhad H, Youssefian L, Harvey N, Tavasoli AR, Saeidian AH, Sotoudeh S, et al. Mutation update: the spectra of PLEC sequence variants and related plectinopathies. Hum Mutat 2022;43:1706–31.

Vahidnezhad H, Youssefian L, Saeidian AH, Uitto J. Phenotypic Spectrum of epidermolysis bullosa: the Paradigm of syndromic versus non-syndromic skin fragility disorders. J Invest Dermatol 2019;139:522–7.

Valencia RG, Mihailovska E, Winter L, Bauer K, Fischer I, Walko G, et al. Plectin dysfunction in neurons leads to tau accumulation on microtubules affecting neuritogenesis, organelle trafficking, pain sensitivity and memory. Neuropathol Appl Neurobiol 2021;47:73–95.

van Tienen FHJ, Lindsey PJ, Kamps MAF, Krapels IP, Ramaekers FCS, Brunner HG, et al. Assessment of fibroblast nuclear morphology aids interpretation of LMNA variants. Eur J Hum Genet 2019;27:389–99.

Vandesompele J, De Preter K, Pattyn F, Poppe B, Van Roy N, De Paepe A, et al. Accurate normalization of real-time quantitative RT-PCR data by geometric averaging of multiple internal control genes. Genome Biol 2002;3:research0034.1.

Vishwanathan GB, Srinivasa M, Batrani M, Kubba A, Ghosh S, Gupta D, et al. Clinical heterogeneity in epidermolysis bullosa simplex with plectin (PLEC) mutations-A study of six unrelated families from India. Am J Med Genet A 2022;188:2454–9.

Vlcek S, Just H, Dechat T, Foisner R. Functional diversity of LAP2alpha and LAP2beta in postmitotic chromosome association is caused by an alpha-specific nuclear targeting domain. EMBO J 1999;18:6370–84.

Wally V, Klausegger A, Koller U, Lochmüller H, Krause S, Wiche G, et al. 5′ trans-splicing repair of the PLEC1 gene. J Invest Dermatol 2008;128:568–74.

Walter MC, Reilich P, Krause S, Hiebeler M, Gehling S, Goebel HH, et al. Congenital myopathy and epidermolysis bullosa due to PLEC variant. Neuromuscul Disord 2021;31:1212–7.

Wiche G. Plectin-mediated intermediate filament functions: why isoforms matter. Cells 2021;10:2154.

Wiche G, Winter L. Plectin isoforms as organizers of intermediate filament cytoarchitecture. BioArchitecture 2011;1:14–20.

Wilhelmsen K, Litjens SH, Kuikman I, Tshimbalanga N, Janssen H, van den Bout I, et al. Nesprin-3, a novel outer nuclear membrane protein, associates with the cytoskeletal linker protein plectin. J Cell Biol 2005;171:799–810.

Winter L, Abrahamsberg C, Wiche G. Plectin isoform 1b mediates mitochondrion-intermediate filament network linkage and controls organelle shape. J Cell Biol 2008;181:903–11.

Winter L, Kuznetsov AV, Grimm M, Zeöld A, Fischer I, Wiche G. Plectin isoform P1b and P1d deficiencies differentially affect mitochondrial morphology and function in skeletal muscle. Hum Mol Genet 2015;24:4530–44.

Winter L, Staszewska I, Mihailovska E, Fischer I, Goldmann WH, Schröder R, et al. Chemical chaperone ameliorates pathological protein aggregation in plectin-deficient muscle. J Clin Invest 2014;124:1144–57.

Winter L, Türk M, Harter PN, Mittelbronn M, Kornblum C, Norwood F, et al. Downstream effects of plectin mutations in epidermolysis bullosa simplex with muscular dystrophy. Acta Neuropathol Commun 2016;4:44.

Wu H, Shen Y, Sivagurunathan S, Weber MS, Adam SA, Shin JH, et al. Vimentin intermediate filaments and filamentous actin form unexpected interpenetrating networks that redefine the cell cortex. Proc Natl Acad Sci USA 2022;119:e2115217119.

Xu R, He S, Ma D, Liang R, Luo Q, Song G. Plectin downregulation inhibits migration and suppresses epithelial mesenchymal transformation of hepatocellular carcinoma cells via ERK1/2 signaling. Int J Mol Sci 2022;24:73.

Yiu EM, Klausegger A, Waddell LB, Grasern N, Lloyd L, Tran K, et al. Epidermolysis bullosa with late-onset muscular dystrophy and plectin deficiency. Muscle Nerve 2011;44:135–41.

Zomer HD, Trentin AG. Skin wound healing in humans and mice: challenges in translational research. J Dermatol Sci 2018;90:3–12.

Zrelski MM, Kustermann M, Winter L. Muscle-Related Plectinopathies. Cells 2021;10:2480.

SUPPLEMENTARY REFERENCES

Bauer JW, Rouan F, Kofler B, Rezniczek GA, Kornacker I, Muss W, et al. A compound heterozygous one amino-acid insertion/nonsense mutation in the plectin gene causes epidermolysis bullosa simplex with plectin deficiency. Am J Pathol 2001;158:617–25.

Brooks J, Fleschner CR. Identification of a vimentin-reactive Peptide associated with ocular lens membranes as cytokeratin. Ophthalmic Res 2003;35:8–11.

Brugè F, Venditti E, Tiano L, Littarru GP, Damiani E. Reference gene validation for qPCR on normoxia- and hypoxia-cultured human dermal fibroblasts exposed to UVA: is beta-actin a reliable normalizer for photoaging studies? J Biotechnol 2011;156:153–62.

Kunz M, Rouan F, Pulkkinen L, Hamm H, Jeschke R, Bruckner-Tuderman L, et al. Mutation reports: epidermolysis bullosa simplex associated with severe mucous membrane involvement and novel mutations in the plectin gene. J Invest Dermatol 2000;114:376–80.

Lammerding J, Hsiao J, Schulze PC, Kozlov S, Stewart CL, Lee RT. Abnormal nuclear shape and impaired mechanotransduction in emerin-deficient cells. J Cell Biol 2005;170:781–91.

Natsuga K, Nishie W, Akiyama M, Nakamura H, Shinkuma S, McMillan JR, et al. Plectin expression patterns determine two distinct subtypes of epidermolysis bullosa simplex. Hum Mutat 2010a;31:308–16.

Nazet U, Schröder A, Grässel S, Muschter D, Proff P, Kirschneck C. Housekeeping gene validation for RT-qPCR studies on synovial fibroblasts derived from healthy and osteoarthritic patients with focus on mechanical loading. PLoS One 2019;14:e0225790.

van Tienen FHJ, Lindsey PJ, Kamps MAF, Krapels IP, Ramaekers FCS, Brunner HG, et al. Assessment of fibroblast nuclear morphology aids interpretation of LMNA variants. Eur J Hum Genet 2019;27:389–99.

Wally V, Klausegger A, Koller U, Lochmüller H, Krause S, Wiche G, et al. 5′ trans-splicing repair of the PLEC1 gene. J Invest Dermatol 2008;128:568–74.

Wei Y, Lv B, Xie J, Zhang Y, Lin Y, Wang S, et al. Plumbagin promotes human hepatoma SMMC-7721 cell apoptosis via caspase-3/vimentin signal-mediated EMT. Drug Des Devel Ther 2019;13:2343–55.

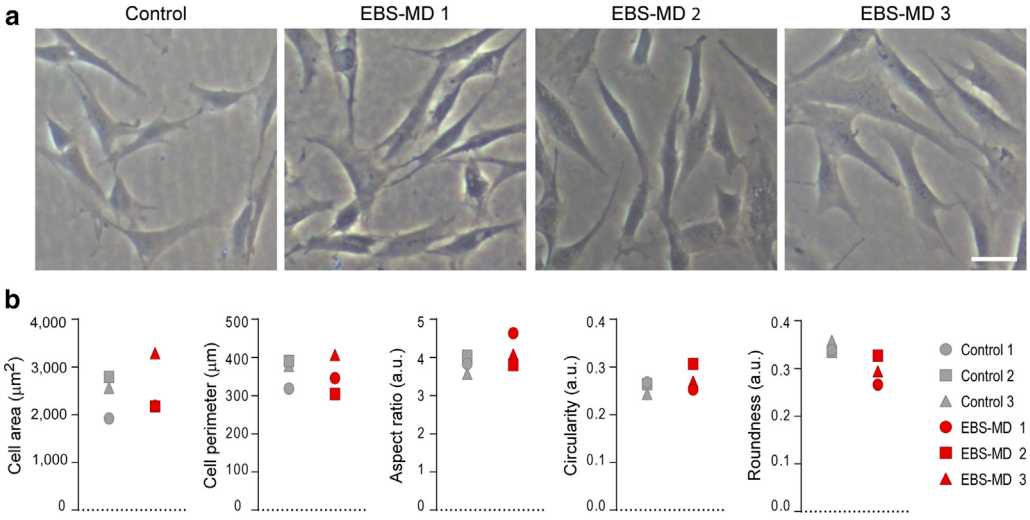

Supplementary Figure S1. Similar cell morphologies of control and EBS-MD fibroblasts. (**a**) Transmitted light microscopic images of control and EBS-MD fibroblasts. Bar = 50 μm. (**b**) Statistical analyses of cell area, perimeter, aspect ratio, circularity, and roundness. Data are presented as mean (control 1 [n = 50 cells], control 2 [n = 44 cells], control 3 [n = 51 cells], EBS-MD 1 [n = 51 cells], EBS-MD 2 [n = 50 cells], and EBS-MD 3 [n = 45 cells]). EBS-MD, epidermolysis bullosa simplex with muscular dystrophy.

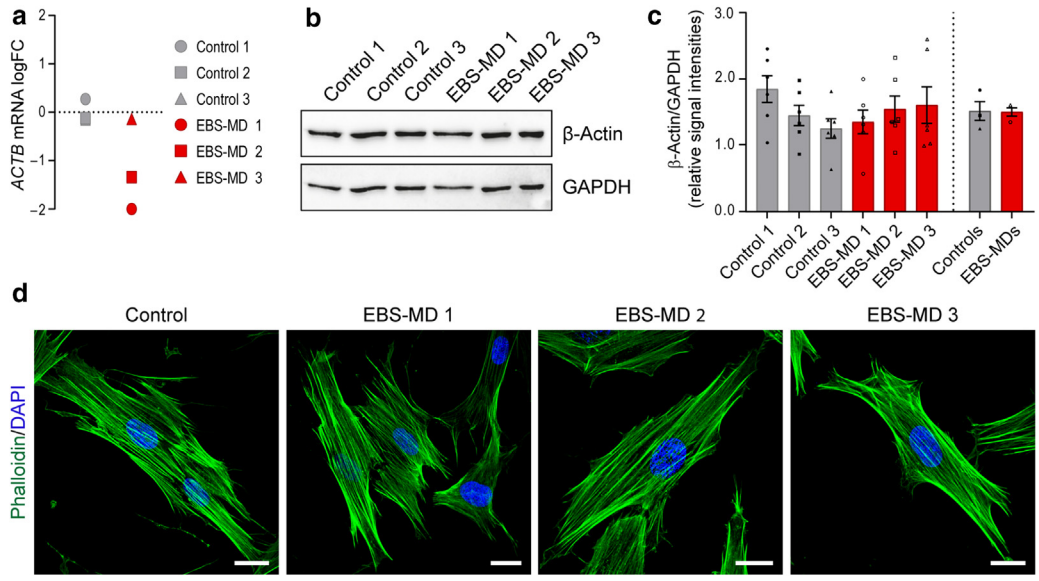

Supplementary Figure S2. No obvious alterations in actin expression or microfilament network architecture in EBS-MD fibroblasts. (**a**) RT-qPCR analyses of β-actin (*ACTB*) mRNA expression. Relative gene expression values are depicted as logFC and were normalized to *TBP* and *RPLP0*. Samples were measured as triplicates. (**b**) Immunoblotting of cell lysates prepared from control and EBS-MD fibroblasts using anti−β-actin antibodies. GAPDH was used as the loading control. (**c**) Signal intensities of β-actin protein bands as shown in **b** were densitometrically measured and normalized to GAPDH. Data are presented as mean ± SEM; n = 6 data points, derived from two independent experiments (at two different passages). (**d**) Actin staining of control and EBS-MD fibroblasts using phalloidin and visualization of nuclei (DAPI). Bars = 20 μm. EBS-MD, epidermolysis bullosa simplex with muscular dystrophy; logFC, $\log_2$ fold change.

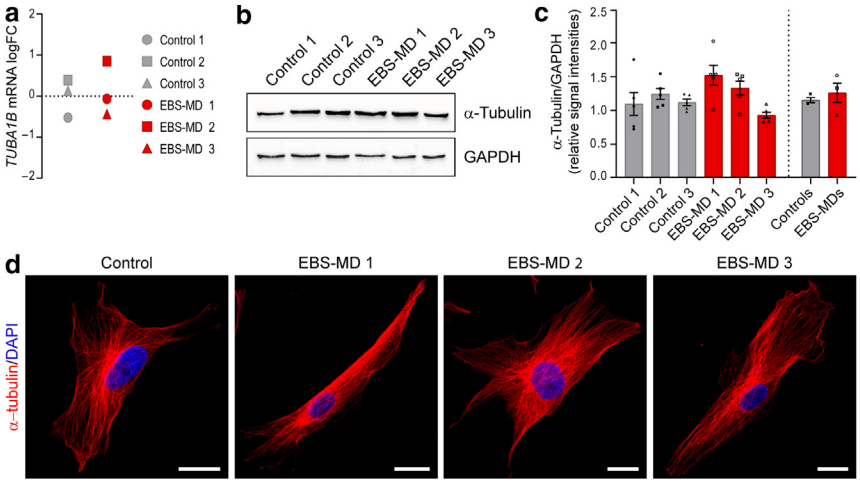

Supplementary Figure S3. No obvious alterations in tubulin expression or microtubule network architecture in EBS-MD fibroblasts. (**a**) RT-qPCR analyses of α-tubulin 1b (*TUBA1B*) mRNA expression. Relative gene expression values are depicted as logFC and were normalized to *TBP* and *RPLP0*. Samples were measured as triplicates. (**b**) Immunoblotting of cell lysates prepared from control and EBS-MD fibroblasts using anti−α-tubulin antibodies. GAPDH was used as the loading control. (**c**) Signal intensities of α-tubulin protein bands as shown in **b** were densitometrically measured and normalized to GAPDH. Data are presented as mean ± SEM; n = 5 data points, derived from two independent experiments (at two different passages). (**d**) Immunostaining of control and EBS-MD fibroblasts using anti−α-tubulin antibodies and visualization of nuclei (DAPI). Bars = 20 μm. EBS-MD, epidermolysis bullosa simplex with muscular dystrophy; logFC, $\log_2$ fold change.

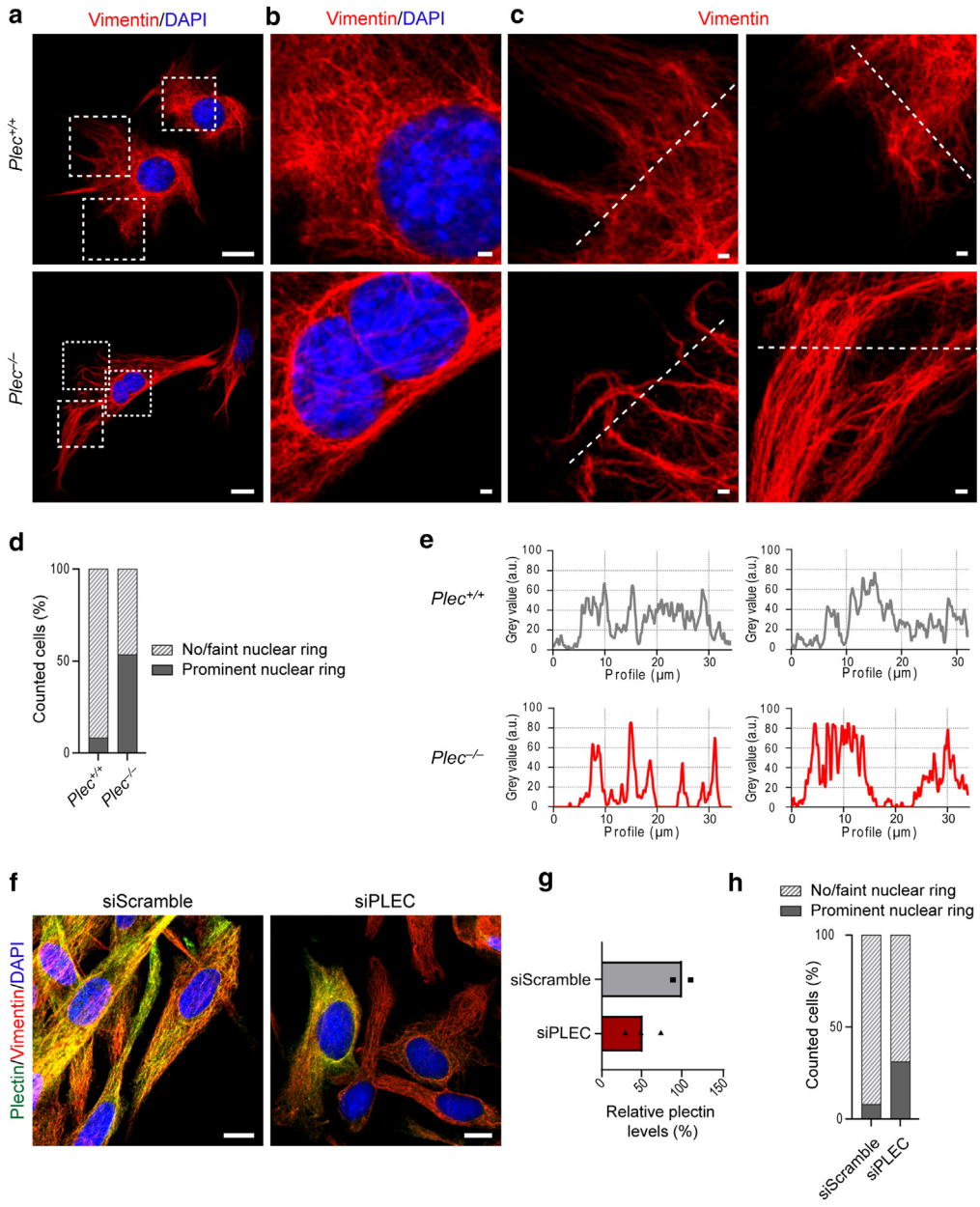

Supplementary Figure S4. Altered intermediate filament network architecture in murine plectin-deficient cells and human control fibroblasts upon plectin knockdown. (**a**–**c**) Immunostaining of immortalized murine plectin-positive (*Plec*$^{+/+}$) and plectin-deficient (*Plec*$^{-/-}$) fibroblasts using antibodies to vimentin and visualization of nuclei (DAPI, for **a**). Boxes indicated in **a** are magnified in **b** and **c**. Note the (**b**) formation of ring-like nuclei-encasing structures and (**c**) highly bundled cable-like vimentin IFs in *Plec*$^{-/-}$ fibroblasts. Bars = 20 μm (**a**) and 2 μm (**b** and **c**). (**d**) Percentage of fibroblasts with or without a prominent nuclear vimentin IF ring (*Plec*$^{+/+}$ [n = 125 cells] and *Plec*$^{-/-}$ [n = 128 cells]), derived from three independent experiments. (**e**) Graphs represent fluorescence intensity profiles illustrating the respective vimentin distributions in *Plec*$^{+/+}$ and *Plec*$^{-/-}$ fibroblasts. The white dashed lines in **c** denote the direction of the profiling. Note the formation of prominent individual peaks and distinct spaces devoid of vimentin signals in *Plec*$^{-/-}$ fibroblasts. (**f**) Immunostaining of human control fibroblasts transfected either with scrambled siRNA (denoted by siScramble) or plectin siRNA (denoted by siPLEC) using antibodies to plectin (green) and to vimentin (red) and visualization of nuclei (DAPI). Note the reduced plectin signals in the siPLEC cells and the coinciding increased bundling of the vimentin IF networks. Bars = 20 μm. (**g**) Quantification of plectin knockdown efficiency by assessment of relative fluorescence signals of the plectin immunostaining (siScramble [n = 119 cells] and siPLEC [n = 157 cells), derived from two independent experiments. (**h**) Percentage of fibroblasts with or without a prominent nuclear vimentin IF ring (siScramble [n = 119 cells] and siPLEC [n = 157 cells]), derived from two independent experiments. a.u., arbitrary unit; IF, intermediate filament; siRNA, small interfering RNA.

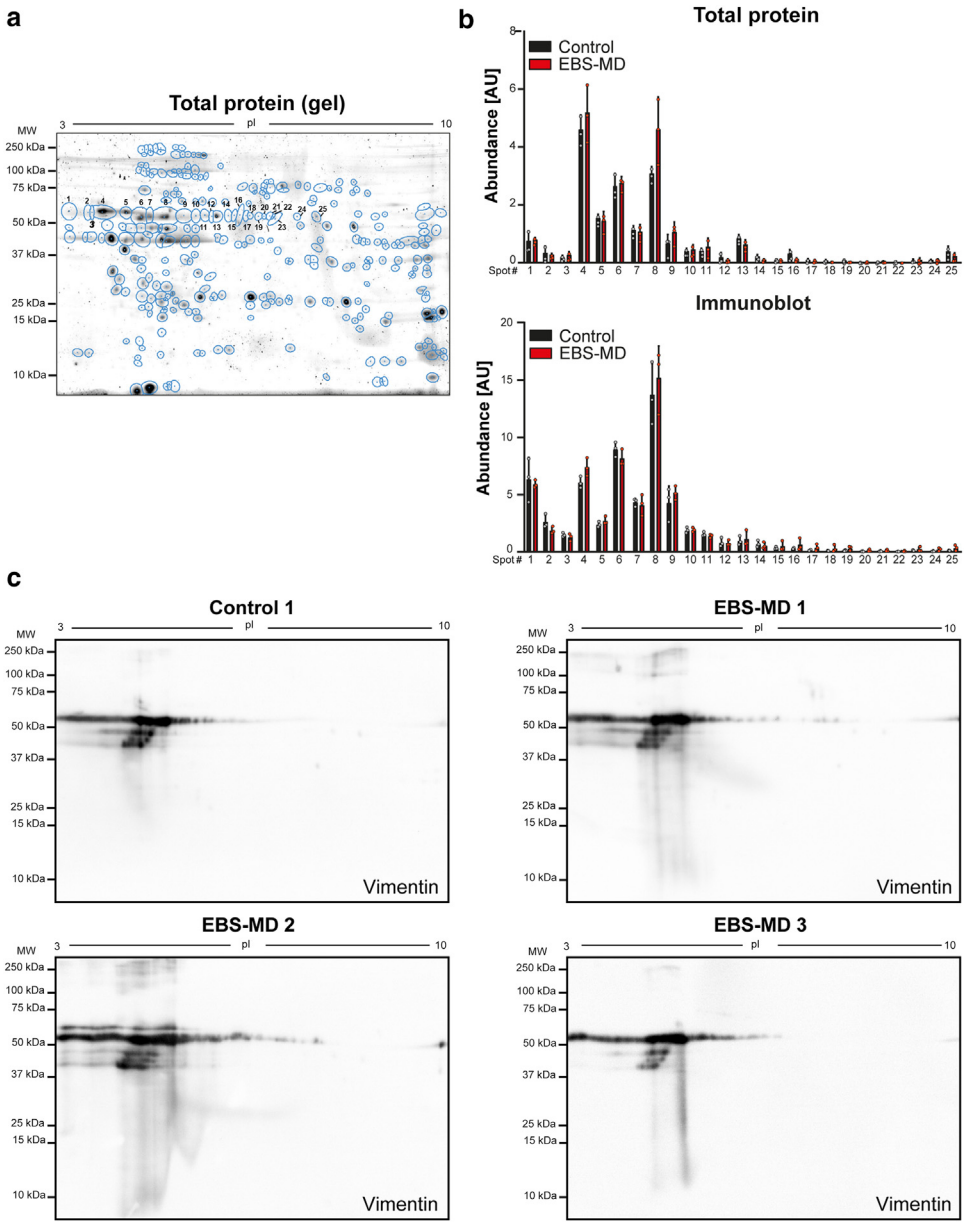

Supplementary Figure S5. 2D immunoblotting analysis of vimentin. (**a**) Total protein 2D gel visualized by stain-free UV detection (fusion image of all conditions) with detected protein spots (n = 292, blue circles); labeled (#1–25) are the spots with signals detected in the vimentin immunoblot (in **c**). (**b**) Mean (±SD) spot density of control (n = 3, black bars) and EBS-MD (n = 3, red bars). (**c**) Representative 2D immunoblots with vimentin signals at 54 kD (signals from 44–50 kD are described as vimentin antibody–caused artifacts seen in 2D immunoblots, especially after lysis with a urea-based buffer [Brooks and Fleschner, 2003]). 2D, two-dimensional; AU, arbitrary unit; EBS-MD, epidermolysis bullosa simplex with muscular dystrophy.

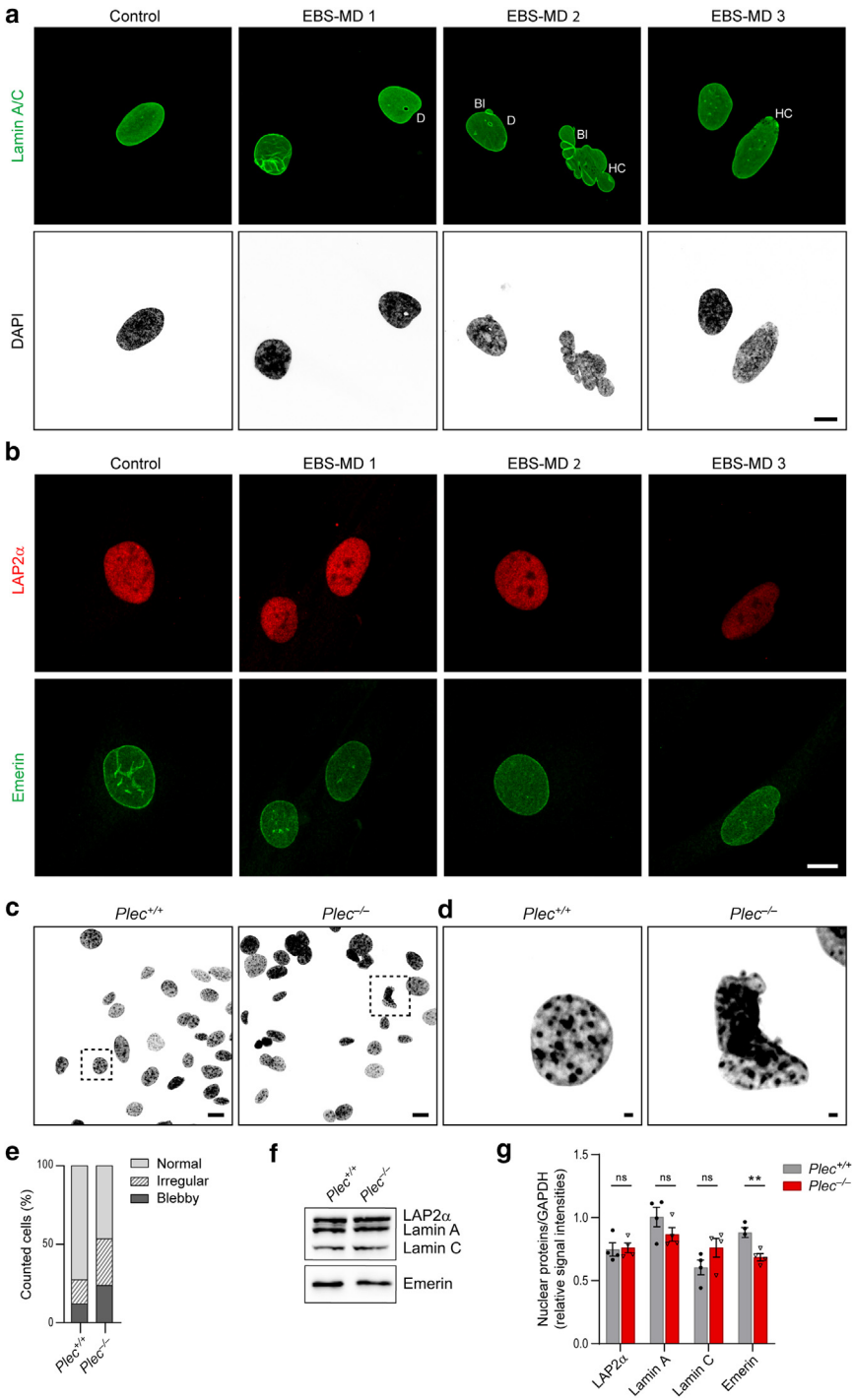

Supplementary Figure S6. Altered nuclear morphology in humans EBS-MD cells and murine *Plec*$^{-/-}$ fibroblasts. (**a, b**) Maximum intensity projections of confocal Z-stacks of immunostained control and EBS-MD fibroblasts using antibodies to (**a**) lamin A/C or (**b**) LAP2α and emerin. Nuclei were stained with DAPI. Note the occurrence of irregularities in the nuclear lamina such as donuts (denoted as D), blebs (denoted as Bl), and honeycomb structures (denoted as HC) (van Tienen et al., 2019). (**c**) Visualization of nuclear morphology (DAPI) in *Plec*$^{+/+}$ and *Plec*$^{-/-}$ mouse fibroblasts. (**d**) Magnifications of the boxed nuclei in c. Note the occurrence of nuclear abnormalities such as irregularly shaped and blebby nuclei in plectin knockout fibroblasts. Bars = 20 μm (for **c**) and 2 μm (for **d**). (**e**) Percentage of cells presenting with normal, irregularly shaped, or blebbing nuclei (Lammerding et al., 2005) (Plec$^{+/+}$ [n = 162 cells] and *Plec*$^{-/-}$ [n = 142 cells from three independent experiments]). (**f**) Immunoblotting of cell lysates prepared from *Plec*$^{+/+}$ and *Plec*$^{-/-}$ fibroblasts using antibodies to nuclear proteins. GAPDH was used as the loading control. (**g**) Signal intensities of protein bands of LAP2α, lamin A, lamin C, and emerin as shown in **f** were densitometrically measured and normalized to GAPDH. Data are presented as mean ± SEM; n = 4 data points, derived from one experiment. $^{**}P < 0.01$, unpaired Student's *t*-test. EBS-MD, epidermolysis bullosa simplex with muscular dystrophy; ns, not significant.

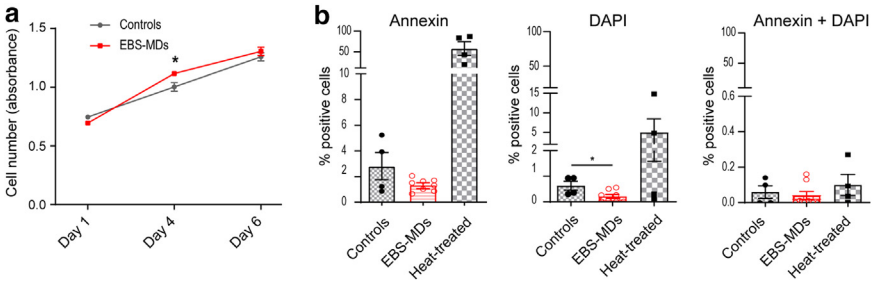

Supplementary Figure S7. Similar proliferation and apoptosis rates of control and EBS-MD fibroblasts. (**a**) Statistical analyses of cell numbers over the course of 6 days. (**b**) Cells were stained with annexin V and DAPI and then visualized with flow cytometry to detect apoptotic cells. Heat-treated (95 °C, 5 min) cells were used as positive control. Note that the number of necrotic cells was significantly reduced in patients with EBS-MD. $*P < 0.05$ (for **a** and **b**) compared with that in control cells; unpaired Student's *t*-test. Each dot represents one measurement; data were derived from two independent experiments. EBS-MD, epidermolysis bullosa simplex with muscular dystrophy; min, minute.

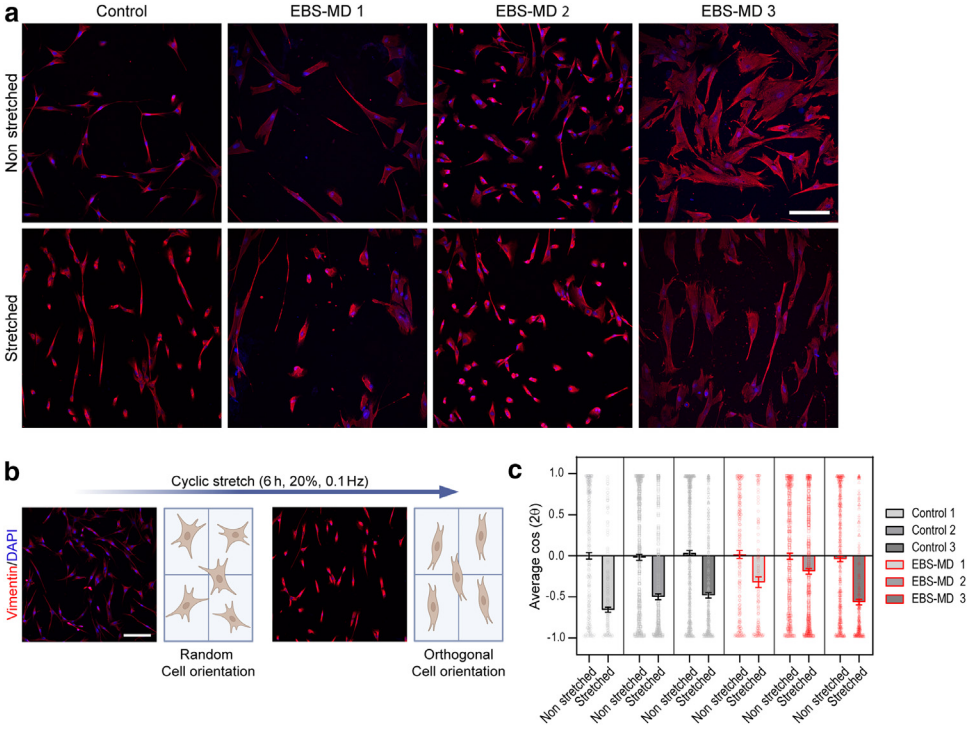

Supplementary Figure S8. Impaired orientation of EBS-MD fibroblast in response to cyclic stretch. (**a**) Immunostaining of control and EBS-MD fibroblasts either nonstretched or after application of cyclic stretch for 6 h (stretched) using antibodies to vimentin (in red). Visualization of nuclei using DRAQ5 (in blue). Bars = 20 μm. (**b**) Micrographs and schemes illustrating the random orientation of cells before and the orthogonal orientation after the application of 20% uniaxial, cyclic stretch at 0.1 Hz for 6 h. Bar = 150 μm. (**c**) Statistical evaluation of the orientation of control and EBS-MD fibroblasts before (nonstretched) or after (stretched) stretch. Orientation was evaluated by fitting an ellipse to each cell and calculating the cos of the respective angle, resulting in values between 1 and −1. Thereby, randomly oriented cells presented with a mean value of 0, whereas cells oriented orthogonal to the direction of the stretch obtained values up to −1. Each dot represents a single cell (control 1 [n = 337/268 nonstretched/stretched cells], control 2 [n = 396/323 nonstretched/stretched cells], control 3 [n = 572/360 nonstretched/stretched cells], EBS-MD 1 [n = 216/127 nonstretched/stretched cells], EBS-MD 2 [n = 356/412 nonstretched/stretched cells], and EBS-MD 3 [n = 458/286 nonstretched/stretched cells]). EBS-MD, epidermolysis bullosa simplex with muscular dystrophy; h, hour.

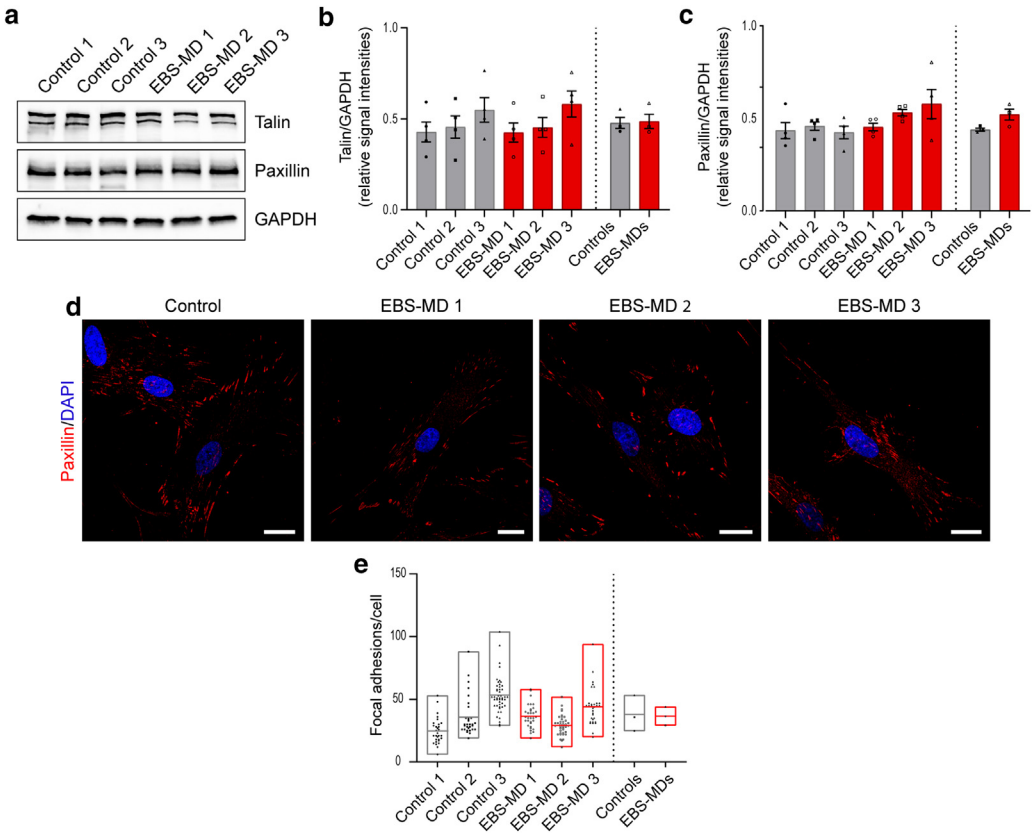

Supplementary Figure S9. Expression levels of talin and paxilin as well as focal adhesion numbers are comparable between control and EBS-MD fibroblasts. (**a**) Immunoblotting of cell lysates prepared from control and EBS-MD fibroblasts using antibodies to talin and to paxillin as indicated. GAPDH was used as the loading control. (**b, c**) Signal intensities of (**b**) talin and (**c**) paxillin protein bands as shown in **a** were densitometrically measured and normalized to GAPDH. Data are presented as mean ± SEM; n = 4 data points, derived from two independent experiments (at two different passages). (**d**) Immunostaining of control and EBS-MD fibroblasts using antibodies to paxillin and visualization of nuclei (DAPI). Bars = 20 μm. (**e**) Numbers of focal adhesions per cell. Floating bar graphs show the mean and the full range of the data (from minimum to maximum). Each dot represents a single cell (control 1 [n = 30 cells], control 2 [n = 31 cells], control 3 [n = 47 cells], EBS-MD 1 [n = 32 cells], EBS-MD 2 [n = 38 cells], and EBS-MD 3 [n = 32 cells]. EBS-MD, epidermolysis bullosa simplex with muscular dystrophy.

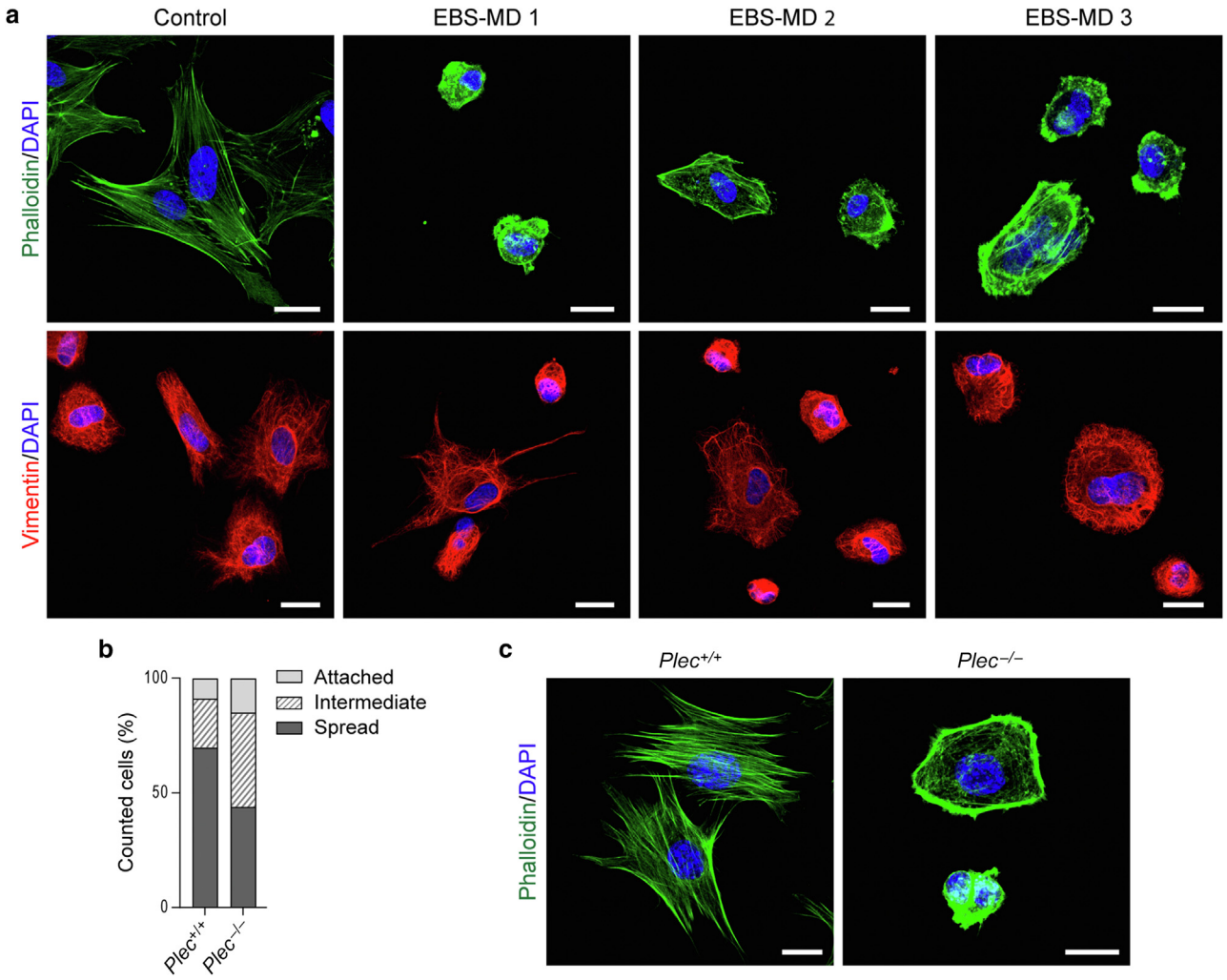

Supplementary Figure S10. Altered actin and IF networks in EBS-MD fibroblasts after 4-h adhesion and impaired adhesion capacities of *Plec*$^{-/-}$ cells. (**a**) Control and EBS-MD fibroblasts 4 h after seeding were stained for actin (upper panel) or vimentin (bottom panel), using phalloidin or antibodies to vimentin. Nuclei were visualized using DAPI. Note the appearance of condensed and highly collapsed actin and vimentin networks in EBS-MD cells. Bars = 20 μm. (**b**) Percentage of attached, intermediate, or spread *Plec*$^{+/+}$ and *Plec*$^{-/-}$ fibroblasts after 4 h of adhesion (*Plec*$^{+/+}$ [n = 157] and *Plec*$^{-/-}$ [n = 107 cells]). (**c**) *Plec*$^{+/+}$ and *Plec*$^{-/-}$ fibroblasts 4 h after seeding were stained for actin using phalloidin. Nuclei were visualized using DAPI. Bar = 20 μm. EBS-MD, epidermolysis bullosa simplex with muscular dystrophy; h, hour; IF, intermediate filament.

Supplementary Table S1. Description of the Localization and Type of Sequence Variation in the *PLEC* Gene

Patients	DNA	Exon	Protein	References
EBS-MD 1	c.4643_4667dup c.7120C>T	Both in exon 31	p.K1558GfsX89 p.Q2374X	Natsuga et al., 2010a
EBS-MD 2	c.5137C>T c.7051C>T	Both in exon 31	p.Q1713X p.R2351X	Kunz et al., 2000; Natsuga et al., 2010a
EBS-MD 3	c.954_956dup c.4222C>T	Exon 9 Exon 31	p.L319dup p.Q1408X	Bauer et al., 2001; Wally et al., 2008

Abbreviation: EBS-MD, epidermolysis bullosa simplex with muscular dystrophy.

Supplementary Table S2. Vimentin Phosphorylation Sites Detected by Mass Spectrometry

			Abundances (Scaled)					
Position in VIM	**Sequence**	**Modification**	**C1**	**C2**	**C3**	**EBS-MD1**	**EBS-MD2**	**EBS-MD3**
P08670 (51–64)	(R) .SLYASSPGGVYATR.(S)	1xPhospho (S6[100])	91	76,2	92,8	118	187,2	34,9
P08670 (403–424)	(K).LLEGEESRISLPLPNFSSLNLR.(E)	1xPhospho (S10[100])	117,4	93,6	117,8	98,5	172,7	—
P08670 (425–439)	(R) .ETNLDSLPLVDTHSK.(R)	1xPhospho (S6[100])	71	53,2	76,8	88,9	185,7	124,4
P08670 (451–466)	(R) .DGQVINETSQHHDDLE.(-)	1xPhospho (S9[99.6])	106,8	70,5	113,6	102,8	176,3	29,9
P08670 (411–424)	(R) .ISLPLPNFSSLNLR.(E)	1xPhospho (S10[99.6])	—	64,8	94,9	119,1	234,4	86,7
P08670 (402–424)	(R) .KLLEGEESRISLPLPNFSSLNLR.(E)	1xPhospho (S)	—	—	—	—	—	—

Abbreviation: EBS-MD, epidermolysis bullosa simplex with muscular dystrophy.

Supplementary Table S3. List of Primers Used for RT-qPCR Analyses

Gene	Forward Primer (5′–3′)	Reverse Primer (5′–3′)	Accession Number	Reference
TBP	5′-CGG CTG TTT AAC TTC GCT TCC-3′	5′-TGG GTT ATC TTC ACA CGC CAA G-3′	NM_003194.4	Nazet et al., 2019
RPLP0	5′-GGA GAC AAA GTG GGA GCC AG-3′	5′-AAC ATT GCG GAC ACC CTC C-3′	NM_001002.4	—
PLEC (rodless)	5′-GTT CAT CAG CGA GAC TCT GC-3′	5′-GCC TTC TCC TGC TCG ATG AA-3′	*NM_000445.5*	—
PLEC (full-length)	5′-GTT CAT CAG CGA GAC TCT GC-3′	5′-CAC CAC CTC CTC CTG CAT G-3′	NM_000445.5	—
ACTB	5′-TCC TTC CTG GGC ATG GAG T-3′	5′-AGC ACT GTG TTG GCG TAC AG-3′	NM_001101.5	Brugè et al., 2011
TUBA1B	5′-GTC GCC TTC GCC TCC TAA TC-3′	5′-CCG TGT TCC AGG CAG TAG AG-3′	NM_006082.3	—
VIM	5′-TGA GTA CCG GAG ACA GGT GCA G-3′	5′-TAG CAG CTT CAA CGG CAA AGT TC-3′	NM_003380.5	Wei et al., 2019